

# Taylor States in Stellarators: A Fast High-order Boundary Integral Solver

Dhairya Malhotra,<sup>\*</sup> Antoine Cerfon,<sup>†</sup> Lise-Marie Imbert-Gérard,<sup>‡</sup>  
and Michael O’Neil<sup>§</sup>

February 22, 2019

## Abstract

We present a boundary integral equation solver for computing Taylor relaxed states in non-axisymmetric solid and shell-like toroidal geometries. The computation of Taylor states in these geometries is a key element for the calculation of stepped pressure stellarator equilibria. The integral representation of the magnetic field in this work is based on the generalized Debye source formulation, and results in a well-conditioned second-kind boundary integral equation. The integral equation solver is based on a spectral discretization of the geometry and unknowns, and the computation of the associated weakly-singular integrals is performed with high-order quadrature based on a partition of unity. The resulting scheme for applying the integral operator is then coupled with an iterative solver and suitable preconditioners. Several numerical examples are provided to demonstrate the accuracy and efficiency of our method, and a direct comparison with the leading code in the field is reported.

**Keywords:** Taylor state, stellarator, generalized Debye sources, plasma equilibria, Laplace-Beltrami

## 1 Introduction

The computation of magnetohydrodynamic (MHD) equilibria in toroidal domains without axisymmetry is a notoriously challenging problem, having both computational roadblocks

---

<sup>\*</sup>Courant Institute of Mathematical Sciences, New York University, 251 Mercer St, New York, NY 10012. *Email:* malhotra@cims.nyu.edu. Research supported in part by the Office of Naval Research under award number #N00014-17-1-2451, the Simons Foundation/SFARI (560651, AB), and the U.S. Department of Energy, Office of Science, Fusion Energy Sciences under Awards No. DE-FG02-86ER53223 and DE-SC0012398

<sup>†</sup>Courant Institute of Mathematical Sciences, New York University, 251 Mercer St, New York, NY 10012. *Email:* cerfon@cims.nyu.edu. Research partially supported by the Simons Foundation/SFARI (560651, AB), and by the U.S. Department of Energy, Office of Science, Fusion Energy Sciences under Awards No. DE-FG02-86ER53223 and DE-SC0012398

<sup>‡</sup>Department of Mathematics, University of Maryland, 4176 Campus Drive, College Park, MD 20742. *Email:* lmig@math.umd.edu. Research supported in part by the Simons Foundation/SFARI (560651, AB), by the Applied Mathematical Sciences Program of the U.S. Department of Energy under contract DEFGO288ER25053 and by the Office of the Assistant Secretary of Defense for Research and Engineering and AFOSR under NSSEFF program award FA9550-10-1-0180.

<sup>§</sup>Courant Institute of Mathematical Sciences, New York University, 251 Mercer St, New York, NY 10012. *Email:* oneil@cims.nyu.edu. Research supported in part by the Office of Naval Research under award numbers #N00014-17-1-2451 and #N00014-17-1-2059.

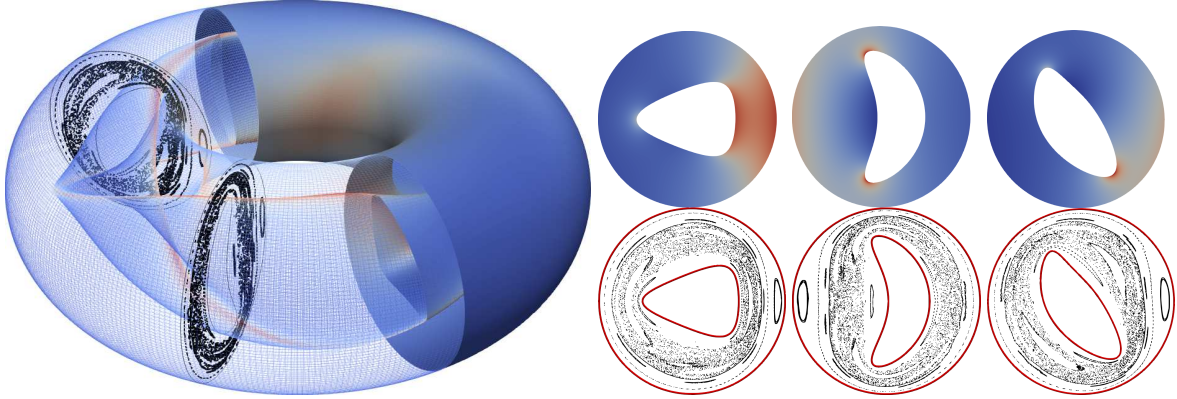


Figure 1: An example of a Taylor state computed in a toroidal-shell domain. Using our boundary integral method, we only need to discretize the domain boundary. This reduces the dimensionality of the unknowns needed, and leads to significant savings in computational work. Once the boundary integral equations are solved, the magnetic field  $\mathbf{B}$  can be evaluated at off-surface points very efficiently. On the right, we show the magnitude of  $\mathbf{B}$  in different cross-sections of the domain as well as Poincaré plots of the field in each cross-section, generated by tracing the field lines using a 10th-order spectral deferred correction (SDC) scheme.

as well as touching on subtle mathematical questions [7, 21, 25, 30]. Until recently, computational efforts to solve this problem could be divided in two categories [23]. The first category of numerical solvers relies on the assumption of the existence of nested magnetic flux surfaces throughout the computational domain [3, 26–28, 52]. These solvers have played an important role in the design of new non-axisymmetric magnetic confinement devices as well as the analysis of experimental results obtained from existing ones. However, they are fundamentally limited in terms of both robustness and accuracy for the computation of equilibria with both a smooth plasma pressure profile and smooth magnetic field line pitch. In this regime, this class of solvers (and the model upon which they are based) is unable to accurately approximate the singular structures in the current density which must naturally occur in such situations [25, 38, 39, 47]. On the other hand, an alternative, second class of solvers, does not constrain the space of solutions to equilibria with nested flux surfaces, and computes equilibria which may have magnetic islands and chaotic magnetic field lines [23, 46, 49]. These solvers also play an important role in the magnetic fusion program since they can be used to study, among other significant questions, the disappearance of magnetic islands, often called *island healing*, corresponding to an increase of the plasma pressure [24, 36] or to a change of the coil configuration [31]. They are also often able to compute the details of the magnetic field configuration in the vicinity of the plasma edge [12]. Despite these additional capabilities, equilibrium codes in the first category are often favored because existing solvers in the second category converge substantially slower [12] and are much more computationally intensive [32].

Recently, a third approach has been developed which combines aspects of the two categories of solvers described above. In this approach, the entire computational domain is subdivided into separate regions, each with constant pressure, assumed to have undergone Taylor relaxation [51] to a minimum energy state subject to conserved fluxes and magnetic helicity. Each of these regions is assumed to be separated by ideal MHD barriers [33, 34]. This model has a significant limitation: for general pressure profiles, solutions of this model

only truly agree with the equations of ideal MHD equilibrium when one takes the limit of infinitely many interfaces [11]. When the number of interfaces is finite, the model is only a first-order approximation of the ideal MHD equilibrium equations, independent of any subsequent numerical discretization. This third approach is nevertheless very promising for several reasons. First, unlike the more general ideal MHD equilibrium case, existence of solutions for the stepped pressure equilibrium model has been established for tori whose departure from axisymmetry is sufficiently small [7]. Second, numerical solvers for this model can be used to study equilibrium configurations with magnetic islands and regions with chaotic magnetic field lines [41] for a computational cost which is substantially smaller than that of ideal MHD solvers having similar capabilities [23, 46, 49]. Furthermore, they generally have more robust convergence properties. Finally, the model is well-suited for rigorous error convergence analysis and code verification [34, 40].

At present time, the only equilibrium code in the third category is known as the Stepped Pressure Equilibrium Code (SPEC) [29]. For a given plasma pressure profile, the computation of equilibria using SPEC is an iterative process. On each iteration, one first computes the magnetic field  $\mathbf{B}$  of the Taylor states inside each region, given by  $\nabla \times \mathbf{B} = \lambda \mathbf{B}$  with  $\lambda$  a specified constant (possibly different in each region). Then, the force-balance condition on the ideal MHD interfaces is verified. If the total pressure  $p + |\mathbf{B}|^2/2$ , where  $p$  is the plasma pressure, is continuous across each interface to the desired numerical precision, the iterative process stops. If it is not continuous to the desired numerical precision, the shape of the MHD interfaces is modified in order to satisfy force balance, and a new iteration starts. This shape optimization is a highly nonlinear procedure.

In this article, we focus on the first step within each iteration, namely the computation of Taylor states given by  $\nabla \times \mathbf{B} = \lambda \mathbf{B}$  in toroidal domains for which the boundary is given, and  $\lambda$  and the flux conditions are such that the problem is well-posed [44]. In SPEC, this is done using a Galerkin approach [34] in which one solves for the magnetic vector potential  $\mathbf{A}$ . The components of  $\mathbf{A}$  are represented using a Fourier-Chebyshev expansion; the Fourier representation captures the double periodicity in the poloidal and toroidal angles and the Chebyshev representation is used for the radial variable [40]. In contrast, in this work we present a boundary integral representation for the Taylor state  $\mathbf{B}$  based on a single scalar variable and solve the associated boundary integral equation. The advantages of our numerical method as compared to the solver in SPEC are the typical advantages one expects from integral equation solvers: the number of unknowns in our approach is much smaller than in SPEC since unknowns are only needed on the surface of the domain, our solver avoids issues with the coordinate singularity which occurs when parameterizing the volume of genus-one domains [33], and the representation immediately leads to a well-conditioned (away from physical interior resonances) second-kind integral equation which can be numerically inverted to high-precision. We will present numerical tests which demonstrate the robustness and efficiency in our approach, showing that for a given target accuracy, our solver is significantly faster than the SPEC code and that it avoids conditioning issues encountered in SPEC.

Our integral equation formulation is based on the same generalized Debye representation that we presented in [44] for the calculation of axisymmetric Taylor states. One may initially think that generalizing the solver from axisymmetric geometries to non-axisymmetric ones is straightforward. This is not so, for several reasons. First, the numerical discretization of the boundary integral equation formulation requires quadratures for weakly-singular ker-

nels on the boundary of the domain. In axisymmetric geometries, the boundary of the domain can merely be considered a closed curve and fast and accurate quadrature schemes are readily available (and easy to implement). However, for the computation of Taylor states in non-axisymmetric geometries, the boundary is a surface; this makes the accurate and fast computation of these integrals much more challenging, both from a mathematical and computational point of view. The same difficulties apply to the computation of the surface gradient and the inverse Laplace-Beltrami operator, which are much easier to evaluate along a closed curve than on general stellarator geometries. Finally, in axisymmetric domains, there exists simple closed form expressions for the surface harmonic vector fields required in our formulation, and this is not the case in non-axisymmetric domains. A significant portion of this article focuses on the new algorithms we developed to address these difficulties. We have implemented our method in the form of a software library called BIEST (Boundary Integral Equation Solver for Taylor states). The library is made publicly available for use by the scientific community and to allow independent verification of our results<sup>1</sup>.

The paper is organized as follows. In Section 2, we present a brief review of the generalized Debye representation for magnetic fields satisfying the Taylor state equation, and of the resulting boundary integral formulation for the computation of the Taylor state. We also give a new numerically stable representation for the computation of the flux condition when  $\lambda$  approaches zero, and present an alternative, more direct method for computing vacuum fields (i.e. the case where  $\lambda = 0$ ). In Section 3 we provide a detailed description of the numerical solver, with a particular emphasis on high-order surface quadratures for singular kernels and inverting the Laplace-Beltrami operator. In Section 4, we test the accuracy and speed of the singular quadrature scheme and of the Laplace-Beltrami solver, as well as the accuracy and speed of the entire solver. In particular, we compare the performance of our solver with that of SPEC for the W7-X geometry [4, 48], a stellarator experiment in Greifswald, Germany. We summarize our work in Section 5 and propose directions for future work.

## 2 Beltrami fields, Taylor states, and generalized Debye sources

In this section we detail the relationship between time harmonic electromagnetic fields and Taylor states. These two classes of vector fields can be directly linked using the generalized Debye integral representation for Taylor states. Using this integral representation, second-kind boundary integral equations are then derived for force-free fields corresponding to Taylor states in stellarator geometries. These boundary integral equations can then be used to solve for stepped-pressure equilibria, as discussed in the introduction.

As discussed in the introduction, in this article we focus solely on the task of computing Taylor states in stellarator geometries. Taylor states are described by the equation

$$\nabla \times \mathbf{B} = \lambda \mathbf{B} \tag{2.1}$$

where  $\lambda$  is a given constant throughout the computational domain, determined based on magnetic energy and helicity. As is well-known [34, 44], this partial differential equation needs boundary conditions and flux constraints on  $\mathbf{B}$  in multiply-connected geometries in order to be well-posed. We will specify them shortly, but refrain from doing so at this stage

---

<sup>1</sup><https://github.com/dmalhotra/BIEST>

in order to focus on the generalized Debye representation for  $\mathbf{B}$  which *a priori* satisfies (2.1), independent of the boundary conditions or the flux constraints.

Since  $\lambda$  is a real-valued constant, it is easy to see that by setting  $\mathbf{E} = i\mathbf{B}$  the pair  $\mathbf{E}, \mathbf{B}$  satisfy the source-free time-harmonic Maxwell equations with wavenumber  $\lambda$ , denoted by THME( $\lambda$ ):

$$\begin{aligned}\nabla \times \mathbf{E} &= i\lambda\mathbf{B}, & \nabla \times \mathbf{B} &= -i\lambda\mathbf{E}, \\ \nabla \cdot \mathbf{E} &= 0, & \nabla \cdot \mathbf{B} &= 0.\end{aligned}\tag{2.2}$$

There is a rich literature on integral equation representations and methods for solving various boundary value problems for the THME( $\lambda$ ). It turns out that the generalized Debye source representation for solutions to the THME is also particularly well-suited for solving boundary value problems for Taylor states [16]. We now turn to a very brief overview of this representation, and the derivation of an integral representation and integral equation for Taylor states in magnetically confined plasmas. Various theoretical and numerical aspects of the generalized Debye source representation can be found in [13, 14, 16, 17, 44].

## 2.1 Generalized Debye sources

An advantage of the generalized Debye source representation is that the fields are constructed so as to automatically satisfy Maxwell's equations, leaving only the boundary condition to be met. This is in contrast to several classical integral representations for electromagnetic fields, as well as virtually all direct PDE discretization schemes (e.g. finite difference and finite element methods).

Denote by  $\Omega$  a domain (bounded or unbounded) with smooth boundary  $\Gamma$ . In  $\Omega$ , any time harmonic electromagnetic field  $\mathbf{E}, \mathbf{H}$  with wavenumber  $k \in \mathbb{C}$  (having nonnegative imaginary part) can be represented using two vector potentials  $\mathbf{A}, \mathbf{Q}$  and two scalar potentials  $u, v$ :

$$\begin{aligned}\mathbf{E} &= ik\mathbf{A} - \nabla u - \nabla \times \mathbf{Q}, \\ \mathbf{H} &= ik\mathbf{Q} - \nabla v + \nabla \times \mathbf{A}.\end{aligned}\tag{2.3}$$

If the vector and scalar potentials satisfy the homogeneous Helmholtz equation in  $\Omega$ , then it is easy to check that the THME( $k$ ) are automatically satisfied so long as:

$$\nabla \cdot \mathbf{A} = ik u, \quad \nabla \cdot \mathbf{Q} = ik v.\tag{2.4}$$

If these potentials are defined by

$$\begin{aligned}\mathbf{A}(\mathbf{x}) &= \int_{\Gamma} g_k(\mathbf{x} - \mathbf{x}') \mathbf{j}(\mathbf{x}') \, da', & u(\mathbf{x}) &= \int_{\Gamma} g_k(\mathbf{x} - \mathbf{x}') \rho(\mathbf{x}') \, da', \\ \mathbf{Q}(\mathbf{x}) &= \int_{\Gamma} g_k(\mathbf{x} - \mathbf{x}') \mathbf{m}(\mathbf{x}') \, da', & v(\mathbf{x}) &= \int_{\Gamma} g_k(\mathbf{x} - \mathbf{x}') \sigma(\mathbf{x}') \, da',\end{aligned}\tag{2.5}$$

where  $g_k(\mathbf{r}) = e^{ik|\mathbf{r}|}/4\pi|\mathbf{r}|$  is the free-space Green's function for the Helmholtz equation in three dimensions and  $da' = da(\mathbf{x}')$  is the differential area element along  $\Gamma$  at the point  $\mathbf{x}'$ , then it can be shown that condition (2.4) is automatically satisfied if the following two consistency conditions are met:

$$\nabla_{\Gamma} \cdot \mathbf{j} = ik\rho, \quad \nabla_{\Gamma} \cdot \mathbf{m} = ik\sigma.\tag{2.6}$$

Above,  $\nabla_\Gamma \cdot \mathbf{j}$  denotes the intrinsic surface divergence of  $\mathbf{j}$  along  $\Gamma$ . With the above formulation, if two scalar boundary conditions are specified (or one vector condition, as is the case in scattering from a perfect electric conductor), the resulting equations for  $u, v, \mathbf{A}, \mathbf{Q}$  are under-determined. To avoid this, and ensure automatic satisfaction of the consistency conditions (2.6), the surface vector fields  $\mathbf{j}, \mathbf{m}$  are explicitly constructed from  $\sigma, \rho$ . The constructions of  $\mathbf{j}, \mathbf{m}$ , referred to as the generalized Debye currents, will vary depending on the boundary conditions being enforced on  $\mathbf{E}, \mathbf{H}$ . For example, in the case of scattering from a perfect electric conductor, the boundary conditions to be met are

$$\mathbf{n} \times \mathbf{E} = \mathbf{F}, \quad \mathbf{n} \cdot \mathbf{H} = g, \quad (2.7)$$

where  $\mathbf{F}$  and  $g$  are data obtained from an incoming electromagnetic field. For these boundary conditions, it has been shown that constructing  $\mathbf{j}, \mathbf{m}$  as

$$\begin{aligned} \mathbf{j} &= ik \left( \nabla_\Gamma \Delta_\Gamma^{-1} \rho - \mathbf{n} \times \nabla_\Gamma \Delta_\Gamma^{-1} \sigma \right) + \mathbf{j}_H, \\ \mathbf{m} &= \mathbf{n} \times \mathbf{j}, \end{aligned} \quad (2.8)$$

leads to a uniquely invertible system of integral equations for the scalar sources  $\sigma, \rho$  and coefficients fixing the projection of  $\mathbf{j}$  onto the subspace of harmonic vectorfields along  $\Gamma$  [13]. Above, we have that  $\nabla_\Gamma$  is the surface gradient operator,  $\Delta_\Gamma^{-1}$  is the inverse of the surface Laplacian (Laplace-Beltrami operator) along  $\Gamma$  restricted to the class of mean-zero functions, and  $\mathbf{j}_H$  is a tangential harmonic vector field along  $\Gamma$  such that  $\nabla_\Gamma \cdot \mathbf{j}_H = 0$  and  $\nabla_\Gamma \cdot \mathbf{n} \times \mathbf{j}_H = 0$ .

The space of harmonic vector fields along  $\Gamma$  has dimension  $2G$ , where  $G$  is the genus of the boundary. In [17, 44], a basis for these harmonic vector fields is known analytically because the boundary  $\Gamma$  is a surface of revolution. However, in the present work, they must be obtained computationally. To do so, we follow a procedure similar to that in [43], which is detailed later on in Section 3.4.

## 2.2 Taylor state formulation

In this section we detail the explicit construction of a vector field  $\mathbf{B}$ , using generalized Debye sources, that *a priori* analytically satisfies the Taylor state equation

$$\nabla \times \mathbf{B} = \lambda \mathbf{B} \quad (2.9)$$

and leads to a uniquely invertible integral equation corresponding to the boundary condition

$$\mathbf{B} \cdot \mathbf{n} = 0. \quad (2.10)$$

For more details on this construction, in general, see [16], and for details in the axisymmetric case see [44]. It should be noted that the above boundary value problem does *not* have a unique solution if  $\lambda$  is an eigenvalue of the curl operator acting on vectorfields with vanishing normal component along the boundary. Furthermore, depending on the particular geometry in which the above boundary value problem is being solved, it must be augmented with a suitable number of extra conditions (usually provided as flux constraints on  $\mathbf{B}$ ) in order to be well-posed. For clarity, the following is a very condensed version of what is contained in the previously mentioned two references.

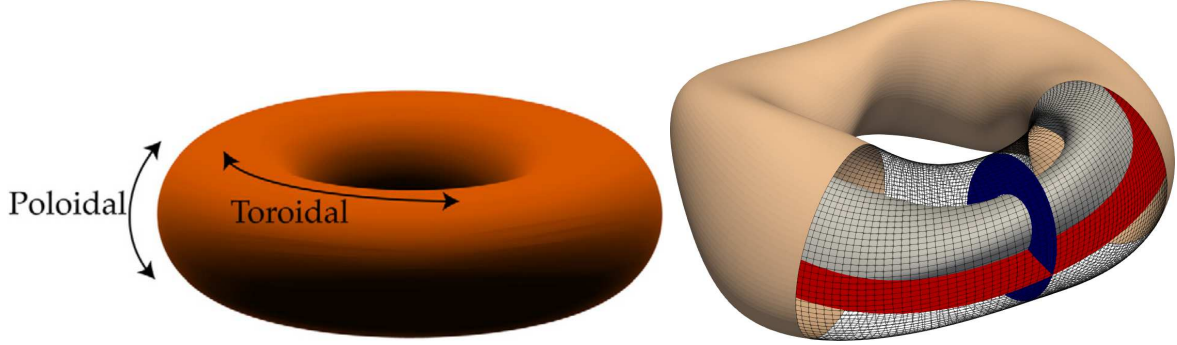


Figure 2: Left: A toroidal surface with the toroidal and poloidal directions. Right: A toroidal shell domain is the region between two nested toroidal geometries. The cross-sections of the domain shown in blue and red are called the toroidal and poloidal cross-sections respectively. The flux conditions for a Taylor state are given as the prescribed magnetic flux through these cross-sections.

### 2.2.1 Generalized Debye representation for Taylor states

For the application at hand, namely that of computing Taylor states for magnetically confined plasmas in general toroidal domains, we must allow for the boundary  $\Gamma$  of the domain  $\Omega$  to be multiply connected, and possibly have multiple components. To this end, let  $\Gamma = \partial\Omega$  be a disjoint union of  $N_s$  smooth toroidal surfaces ( $\Gamma_1, \Gamma_2, \dots, \Gamma_{N_s}$ ). We want to compute vector fields  $\mathbf{B}$  in  $\Omega$  such that,

$$\begin{aligned} \nabla \times \mathbf{B} &= \lambda \mathbf{B}, & \text{in } \Omega, \\ \mathbf{B} \cdot \mathbf{n} &= 0, & \text{on } \Gamma, \\ \int_{S_i} \mathbf{B} \cdot d\mathbf{a} &= \Phi_i & \text{for } i = 1, \dots, N_s, \end{aligned} \quad (2.11)$$

where  $\lambda$  is a constant real number called the Beltrami parameter and  $\mathbf{n}$  is the unit normal vector to  $\Gamma$  pointing outward from  $\Omega$ . The surfaces  $S_i$  are generally chosen to capture all possible toroidal and poloidal fluxes of interest inside  $\Omega$ . In these flux integrals,  $d\mathbf{a} = \mathbf{n} da$  with  $da$  being the surface area element and  $\mathbf{n}$  the oriented normal along the cross-section  $S_i$ . In [44], we applied the generalized Debye representation of [14] for computing Taylor states in axisymmetric geometries. We use the same integral formulation in the present work for computing Taylor states in non-axisymmetric geometries.

As noted before, a vector field  $\mathbf{B}$  which satisfies the Beltrami condition  $\nabla \times \mathbf{B} = \lambda \mathbf{B}$  admits the pair  $(\mathbf{E} = i\mathbf{B}, \mathbf{H} = \mathbf{B})$  which automatically satisfies the THME( $\lambda$ ). The vector field  $\mathbf{B}$  can therefore be represented using the generalized Debye source representation. Furthermore, due to the relation  $\mathbf{E} = i\mathbf{H}$  and the symmetry of the generalized Debye representation in Eq. (2.3), similar dependencies on the vector potentials, scalar potentials, Debye currents, and Debye sources can also be shown [16]:

$$\mathbf{A} = i\mathbf{Q}, \quad u = iv, \quad \rho = i\sigma. \quad (2.12)$$

As a result, the generalized Debye source representation for the Taylor state  $\mathbf{B}$  is given as:

$$\mathbf{B} = i\lambda \mathbf{Q} - \nabla v + i\nabla \times \mathbf{Q}, \quad (2.13)$$

where the vector potential  $\mathbf{Q}$  and the scalar potential  $v$  are as defined before in Eq. (2.5). In order to satisfy  $\nabla \times \mathbf{B} = \lambda \mathbf{B}$ , the consistency condition  $\nabla_\Gamma \cdot \mathbf{m} = i\lambda\sigma$  must be met. With an additional constraint  $\mathbf{n} \times \mathbf{m} = -i \mathbf{m}$ , the surface vector field  $\mathbf{m}$  is determined uniquely up to an additive harmonic vector field,

$$\mathbf{m} = \mathbf{m}_0(\sigma) + \mathbf{m}_H, \quad (2.14)$$

where

$$\mathbf{m}_0(\sigma) = i\lambda \left( \nabla_\Gamma \Delta_\Gamma^{-1} \sigma + i \mathbf{n} \times \nabla_\Gamma \Delta_\Gamma^{-1} \sigma \right) \quad (2.15)$$

and  $\mathbf{m}_H$  is a harmonic surface vector field such that:  $\nabla_\Gamma \cdot \mathbf{m}_H = 0$  and  $\mathbf{n} \times \mathbf{m}_H = -i \mathbf{m}_H$ . As described at the beginning of this section, there are  $N_s$  linearly independent harmonic vector fields  $\{\mathbf{m}_H^1, \dots, \mathbf{m}_H^{N_s}\}$  on  $\Gamma$  satisfying these conditions. Therefore, we may represent  $\mathbf{m}_H$  as:

$$\mathbf{m}_H(\boldsymbol{\alpha}) = \sum_{k=1}^{N_s} \alpha_k \mathbf{m}_H^k. \quad (2.16)$$

The unknowns  $\sigma$  and  $\boldsymbol{\alpha} = \{\alpha_1, \dots, \alpha_{N_s}\}$  must be determined using the boundary conditions and flux constraints in Eq. (2.11).

## 2.2.2 Boundary integral formulation

The generalized Debye representation for  $\mathbf{B}$ , as stated in Eqs. (2.13–2.16), *a priori* satisfies  $\nabla \times \mathbf{B} = \lambda \mathbf{B}$ . However, it does not automatically satisfy the boundary condition  $\mathbf{B} \cdot \mathbf{n} = 0$  on  $\Gamma$ , nor the non-trivial flux constraints. For any scalar function  $\sigma$  and coefficients vector  $\boldsymbol{\alpha}$ , the field  $\mathbf{B}$  can be evaluated directly on the boundary  $\Gamma$  by taking the limit of its value from the interior of  $\Omega$ :

$$\mathbf{B}(\sigma, \boldsymbol{\alpha}) = -\frac{\sigma}{2} \mathbf{n} + i \frac{\mathbf{n} \times \mathbf{m}}{2} + i\lambda \mathcal{S}_\lambda[\mathbf{m}] - \nabla \mathcal{S}_\lambda[\sigma] + i \nabla \times \mathcal{S}_\lambda[\mathbf{m}] \quad \text{on } \Gamma, \quad (2.17)$$

where  $\mathbf{m}(\sigma, \boldsymbol{\alpha})$  is as defined in Eqs. (2.14–2.16) and  $\mathcal{S}_\lambda$  is the single-layer potential operator,

$$\mathcal{S}_\lambda[f](x) = \int_\Gamma g_\lambda(\mathbf{x} - \mathbf{x}') f(\mathbf{x}') da(\mathbf{x}').$$

The boundary condition  $\mathbf{B} \cdot \mathbf{n} = 0$  on  $\Gamma$  results in a second-kind integral equation,

$$-\frac{\sigma}{2} + \mathcal{K}[\sigma, \boldsymbol{\alpha}] = 0, \quad (2.18)$$

where  $\mathcal{K}$  denotes the compact operator,

$$\mathcal{K}[\sigma, \boldsymbol{\alpha}] = i\lambda \mathbf{n} \cdot \mathcal{S}_\lambda[\mathbf{m}] - \partial_n \mathcal{S}_\lambda[\sigma] + i \mathbf{n} \cdot \nabla \times \mathcal{S}_\lambda[\mathbf{m}]. \quad (2.19)$$

## 2.2.3 Flux computation

The flux constraints as stated in Eq. (2.11) are difficult to impose in a boundary integral formulation since we only discretize the boundary  $\Gamma$  and not all of  $\Omega$ . However, using Stokes' theorem and the fact that by construction  $\nabla \times \mathbf{B} = \lambda \mathbf{B}$ , we can relate the flux of  $\mathbf{B}$

through a cross-section  $S$  with its circulation on  $\partial S = S \cap \Gamma$ . Applying the Stokes' theorem and using Eq. (2.17),

$$\begin{aligned}
\int_S \mathbf{B}(\sigma, \boldsymbol{\alpha}) \cdot d\mathbf{a} &= \frac{1}{\lambda} \oint_{\partial S} \mathbf{B}(\sigma, \boldsymbol{\alpha}) \cdot d\mathbf{l} \\
&= \oint_{\partial S} i\mathcal{S}_\lambda[\mathbf{m}_0 + \mathbf{m}_H] \cdot d\mathbf{l} + \frac{i}{\lambda} \oint_{\partial S} \left( \frac{\mathbf{n} \times \mathbf{m}_0}{2} + \nabla \times \mathcal{S}_\lambda[\mathbf{m}_0] \right) \cdot d\mathbf{l} \\
&\quad + \frac{i}{\lambda} \oint_{\partial S} \left( \frac{\mathbf{n} \times \mathbf{m}_H}{2} + \nabla \times \mathcal{S}_\lambda[\mathbf{m}_H] \right) \cdot d\mathbf{l},
\end{aligned} \tag{2.20}$$

where  $\mathbf{m}_0(\sigma)$  is as defined in Eq. (2.15),  $\mathbf{m}_H(\boldsymbol{\alpha})$  is as defined in Eq. (2.16) and  $d\mathbf{l}$  is the oriented unit arclength differential. The first and the second integral terms in Eq. (2.20) remain bounded as  $\lambda \rightarrow 0$  since  $\mathbf{m}_0 \sim \mathcal{O}(\lambda)$ ; however, computing the last term becomes numerically unstable due to the  $1/\lambda$  factor. In order to numerically stabilize this calculation, we begin with the following lemma.

**Lemma 1.** *For a tangential vector field  $\mathbf{m}$  on  $\Gamma$  such that  $\nabla_\Gamma \cdot \mathbf{m} = 0$ , and an arbitrary cross section  $S$  of the domain  $\Omega$ ,*

$$\oint_{\partial S} \left( \frac{\mathbf{n} \times \mathbf{m}}{2} + \nabla \times \mathcal{S}_0[\mathbf{m}] \right) \cdot d\mathbf{l} = 0.$$

*Proof.* Let  $\mathbf{V} = \nabla \times \mathcal{S}_0[\mathbf{m}]$ . Then, at every point in  $\Omega$ , in particular for points on  $S \subset \Omega$ , we have that

$$\begin{aligned}
\nabla \times \mathbf{V} &= \nabla \times \nabla \times \mathcal{S}_0[\mathbf{m}] \\
&= \nabla (\nabla \cdot \mathcal{S}_0[\mathbf{m}]) - \Delta \mathcal{S}_0[\mathbf{m}] \\
&= \nabla \mathcal{S}_0[\nabla_\Gamma \cdot \mathbf{m}] \\
&= 0.
\end{aligned}$$

Furthermore, we have that the limiting value of  $\mathbf{V}$  on  $\partial S$  is

$$\mathbf{V} = \frac{\mathbf{n} \times \mathbf{m}}{2} + \nabla \times \mathcal{S}_0[\mathbf{m}],$$

as in Eq. (2.17). Therefore, by Stokes' theorem

$$\begin{aligned}
\oint_{\partial S} \left( \frac{\mathbf{n} \times \mathbf{m}}{2} + \nabla \times \mathcal{S}_0[\mathbf{m}] \right) \cdot d\mathbf{l} &= \oint_{\partial S} \mathbf{V} \cdot d\mathbf{l} \\
&= \int_S \nabla \times \mathbf{V} \cdot d\mathbf{a} \\
&= 0.
\end{aligned}$$

□

Returning to the previous flux calculation, since  $\nabla_\Gamma \cdot \mathbf{m}_H = 0$  we can apply the above lemma to obtain:

$$\frac{i}{\lambda} \oint_{\partial S} \left( \frac{\mathbf{n} \times \mathbf{m}_H}{2} + \nabla \times \mathcal{S}_0[\mathbf{m}_H] \right) \cdot d\mathbf{l} = 0. \quad (2.21)$$

Subtracting this identity from the last term in Eq. (2.20) gives us the following relation,

$$\frac{1}{\lambda} \oint_{\partial S} \left( \frac{\mathbf{m}_H}{2} + i\nabla \times \mathcal{S}_\lambda[\mathbf{m}_H] \right) \cdot d\mathbf{l} = \oint_{\partial S} i\nabla \times \left( \frac{\mathcal{S}_\lambda - \mathcal{S}_0}{\lambda} \right) [\mathbf{m}_H] \cdot d\mathbf{l}, \quad (2.22)$$

where the operator  $\left( \frac{\mathcal{S}_\lambda - \mathcal{S}_0}{\lambda} \right)$  is equivalent to computing a convolution along the boundary with the following bounded kernel function:

$$\frac{g_\lambda(\mathbf{r}) - g_0(\mathbf{r})}{\lambda} = -\frac{\sin(\lambda|\mathbf{r}|/2) \operatorname{sinc}(\lambda|\mathbf{r}|/2)}{4\pi} + i \frac{\operatorname{sinc}(\lambda|\mathbf{r}|)}{4\pi}.$$

The above expression is obtained straightforwardly using trigonometric identities, and is numerically stable and bounded in its evaluation, even as  $\lambda|\mathbf{r}| \rightarrow 0$ . Therefore, the right hand side in Eq. (2.22) can be stably computed for any value of  $\lambda$ . Using Eqs. (2.20, 2.22), the flux constraints can be re-written as

$$\oint_{\partial S_i} i\mathcal{S}_\lambda[\mathbf{m}_0 + \mathbf{m}_H] \cdot d\mathbf{l} + \frac{1}{\lambda} \oint_{\partial S_i} \left( \frac{\mathbf{m}_0}{2} + i\nabla \times \mathcal{S}_\lambda[\mathbf{m}_0] \right) \cdot d\mathbf{l} + \oint_{\partial S_i} i\nabla \times \left( \frac{\mathcal{S}_\lambda - \mathcal{S}_0}{\lambda} \right) [\mathbf{m}_H] \cdot d\mathbf{l} = \Phi_i, \quad (2.23)$$

for  $i = 1, \dots, N_s$ . The complete formulation for computing Taylor states is given by the boundary integral equation Eq. (2.18) and the flux conditions Eq. (2.23). We will discuss how to discretize and solve these equations to obtain the required numerical solution in Section 3.

#### 2.2.4 Vacuum fields

We now briefly discuss the special case where  $\lambda = 0$ . The magnetic field  $\mathbf{B}$  then satisfies  $\nabla \times \mathbf{B} = \mathbf{0}$ , i.e. it is a vacuum field. In this case, the boundary limit of the integral representation in Eq. (2.17) for  $\mathbf{B}$  simplifies to

$$\mathbf{B}(\sigma, \boldsymbol{\alpha}) = -\frac{\sigma}{2} \mathbf{n} + \frac{\mathbf{m}_H}{2} - \nabla \mathcal{S}_0[\sigma] + i\nabla \times \mathcal{S}_0[\mathbf{m}_H] \quad \text{on } \Gamma, \quad (2.24)$$

where  $\mathbf{m}_H(\boldsymbol{\alpha})$  is as defined in Eq. (2.16). The boundary condition  $\mathbf{B} \cdot \mathbf{n} = 0$  on  $\Gamma$  results in the following second-kind integral equation,

$$-\frac{\sigma}{2} + \mathcal{K}[\sigma, \boldsymbol{\alpha}] = 0, \quad (2.25)$$

where  $\mathcal{K}$  is a compact boundary integral operator given by,

$$\mathcal{K}[\sigma, \boldsymbol{\alpha}] = -\partial_n \mathcal{S}_0[\sigma] + i\mathbf{n} \cdot \nabla \times \mathcal{S}_0[\mathbf{m}_H]. \quad (2.26)$$

The flux constraints in Eq. (2.23) cannot be used directly for vacuum fields since we must first explicitly compute the limit  $\lambda \rightarrow 0$ . To avoid this tedious calculation, we propose a more

straightforward method. We begin by defining a surface vector field  $\mathbf{j} = \mathbf{n} \times \mathbf{B}$  along  $\Gamma$ , and then by using a Green's theorem for magnetostatic fields [10] we obtain that  $\mathbf{B} = \nabla \times \mathcal{S}_0[\mathbf{j}]$  in  $\Omega$ . Notice that  $\mathbf{j}$  is not the same as  $\mathbf{m}_H$ . This relation allows us to use Stokes' theorem to compute the flux of  $\mathbf{B}$  through a cross section  $S$  as the circulation of  $\mathcal{S}_0[\mathbf{j}]$  on  $\partial S$ . The flux constraints can then be written as,

$$\int_S \mathbf{B} \cdot d\mathbf{a} = \oint_{\partial S} \mathcal{S}_0[\mathbf{j}(\sigma, \boldsymbol{\alpha})] \cdot d\mathbf{l} = \Phi_i. \quad (2.27)$$

We discretize and solve Eqs. (2.25, 2.27) for the unknowns  $\sigma$  and  $\boldsymbol{\alpha}$ . This is discussed in the next section. The magnetic field  $\mathbf{B}$  on  $\Gamma$  can then be computed using Eq. (2.24). Notice that in this formulation we do not need to solve a Laplace-Beltrami problem to evaluate the boundary integral operator  $\mathcal{K}$ , and the surface convolution operator  $\mathcal{S}_0$  computes convolutions with the single-layer Laplace kernel which is much less expensive to compute than the Helmholtz kernel.

### 3 A fully 3D Taylor-state solver

In this section, we describe a solver for computing Taylor states in 3D based on the integral equation formulation of the previous section. We give a brief overview of the algorithm in Section 3.1, and then discuss its building blocks: the singular quadrature algorithm in Section 3.2, the spectral Laplace-Beltrami solver in Section 3.3, and the computation of harmonic vector fields in Section 3.4. Finally, we summarize the overall algorithm in Section 3.5.

#### 3.1 An overview of the algorithm

We now give a brief overview of our method. We discuss the scheme used for discretizing the boundary data and define the discretized operators acting on this data, and then discuss how to solve the resulting discretized linear system.

##### 3.1.1 Discretization

One significant advantage that the boundary integral formulation of the previous section has over standard PDE formulations is that only the surface of the domain  $\Omega$  needs to be discretized, yielding an immediate dimension reduction in the number of unknowns. As discussed in Section 2.2, the boundary is a disjoint union of  $N_s$  toroidal (i.e. doubly-periodic) surfaces. We parameterize each surface  $\Gamma_i$  by a pair of toroidal and poloidal angles  $(\theta, \varphi) \in [0, 2\pi)^2$ , and each surface  $\Gamma_i$  is parameterized using a doubly periodic function  $x_i(\theta, \varphi) \in \Gamma_i$ . Similarly, any function  $f$  along the boundary  $\Gamma_i$  can also be parameterized by the toroidal and poloidal angles so that  $f(\theta, \varphi) = f(x_i(\theta, \varphi))$ . We assume that the surface geometry and the parametrization is oriented and non-degenerate such that  $\det \mathbf{G}(\theta, \varphi) > 0$  for all  $(\theta, \varphi) \in [0, 2\pi)^2$ , where  $\mathbf{G}$  is the metric tensor.

We discretize each surface by sampling on a uniform grid of points in the parameter space. The discretization of a function  $f$  along a toroidal surface is denoted by  $\mathbf{f}$  and is obtained by sampling the function on an  $N_\theta \times N_\varphi$  uniform grid,

$$f_{ij} = f(\theta_i, \varphi_j) \quad \text{for } i = 0, \dots, N_\theta - 1 \text{ and } j = 0, \dots, N_\varphi - 1,$$

where  $\theta_i = 2\pi i/N_\theta$  and  $\varphi_j = 2\pi j/N_\varphi$ . Spectrally accurate Fourier approximations of smooth functions  $f$  can then be obtained by computing the expansion

$$f(\theta, \varphi) \approx \sum_{n=0}^{N_\theta-1} \sum_{m=0}^{N_\varphi-1} \widehat{\mathbf{f}}_{nm} e^{i(n\theta+m\varphi)},$$

where the coefficients  $\widehat{\mathbf{f}}_{nm}$  are computed from the grid values through a discrete Fourier transform,

$$\widehat{\mathbf{f}}_{nm} = \frac{1}{2\pi N_\theta N_\varphi} \sum_{i=0}^{N_\theta-1} \sum_{j=0}^{N_\varphi-1} \mathbf{f}_{ij} e^{i(n\theta_i+m\varphi_j)}.$$

We will denote this Fourier transform operation by  $\widehat{\mathbf{f}} = \mathcal{F}\mathbf{f}$  and the inverse operation by  $\mathbf{f} = \mathcal{F}^{-1}\widehat{\mathbf{f}}$ . This scheme is used to approximate the surface geometry  $\mathbf{x}(\theta, \varphi)$ , discretize the unknown  $\sigma(\theta, \varphi)$  in our boundary integral formulation, and obtain the final solution  $\mathbf{B}(\theta, \varphi)$  on the boundary. We will use  $N$  to denote the total number of discretization points across all surfaces  $\{\Gamma_1, \dots, \Gamma_{N_s}\}$ . This discretization scheme of our boundary integral formulation Eq. (2.18) results in a pseudo-spectral Nyström-like discretization scheme where the unknowns are point-values of  $\sigma$  and the boundary conditions are enforced point-wise at the  $N$  surface discretization points, but intermediate operations (e.g. forming the system matrix) are carried out spectrally.

### 3.1.2 Pseudo-spectral differentiation

Our discretization scheme allows us to easily compute derivatives of functions on toroidal surfaces through diagonal operators acting on the Fourier coefficients at a modest loss of numerical accuracy. Therefore, for a function  $f(\theta, \varphi)$  with discretization  $\mathbf{f}$  on an  $N_\theta \times N_\varphi$  grid and with the Fourier coefficients given by  $\widehat{\mathbf{f}} = \mathcal{F}\mathbf{f}$ , we can compute

$$(\widehat{\mathbf{f}}_\theta)_{nm} = i n \widehat{\mathbf{f}}_{nm}, \quad (\widehat{\mathbf{f}}_\varphi)_{nm} = i m \widehat{\mathbf{f}}_{nm}$$

where  $\widehat{\mathbf{f}}_\theta$  and  $\widehat{\mathbf{f}}_\varphi$  are the Fourier coefficients for  $\partial f/\partial\theta$  and  $\partial f/\partial\varphi$  respectively. The derivatives on the regular  $N_\theta \times N_\varphi$  grid can then be evaluated using the inverse Fourier transform,  $\mathbf{f}_\theta = \mathcal{F}^{-1}\widehat{\mathbf{f}}_\theta$  and  $\mathbf{f}_\varphi = \mathcal{F}^{-1}\widehat{\mathbf{f}}_\varphi$ . We will denote the spectral differentiation operators by the notation  $\mathbf{f}_\theta = \mathbf{D}_\theta\mathbf{f}$  and  $\mathbf{f}_\varphi = \mathbf{D}_\varphi\mathbf{f}$ . When implemented using the Fast Fourier Transform (FFT), these operators require  $\mathcal{O}(N \log N)$  work for discretizations on grids with  $N$  points. In our implementation, we use the multithreaded FFTW library [19] to efficiently compute the Fourier transform and its inverse.

For a boundary  $\Gamma$  with the discretized surface points given by  $\mathbf{x}$ , the pseudo-spectral differentiation operators can be used to compute tangent vectors evaluated at the discretization points,

$$\mathbf{x}_\theta = \mathbf{D}_\theta\mathbf{x}, \quad \text{and} \quad \mathbf{x}_\varphi = \mathbf{D}_\varphi\mathbf{x}.$$

We can then also compute the normal vector  $\mathbf{n}$  and the metric tensor  $\mathbf{G}$  at each discretization point on the surface. We start from the continuous expressions,

$$\mathbf{n} = \frac{\mathbf{x}_\theta \times \mathbf{x}_\varphi}{\|\mathbf{x}_\theta \times \mathbf{x}_\varphi\|} \quad \text{and} \quad \mathbf{G} = \begin{bmatrix} \|\mathbf{x}_\theta\|^2 & \mathbf{x}_\theta \cdot \mathbf{x}_\varphi \\ \mathbf{x}_\theta \cdot \mathbf{x}_\varphi & \|\mathbf{x}_\varphi\|^2 \end{bmatrix}, \quad (3.1)$$

where  $\mathbf{x}_\theta = \partial_\theta \mathbf{x}$  and  $\mathbf{x}_\varphi = \partial_\varphi \mathbf{x}$  are the continuous surface tangent vectors. Evaluating the expressions above pointwise for each discretization grid point and for the corresponding components of  $\mathbf{x}_\theta$  and  $\mathbf{x}_\varphi$  gives the discrete vector  $\mathbf{n}$  and discrete metric tensor  $\mathbf{G}$ . If necessary, we flip the direction of the normal vectors so that they always point outward from the domain  $\Omega$  (this is not necessary if the parameterization of  $\Gamma$  was properly oriented). We will use  $\mathbf{n}$  and  $\mathbf{G}$  to construct the discretized operators required in our boundary integral formulation.

### 3.1.3 Discretized operators

The boundary integral formulation of this work requires that we discretize the linear compact operator  $\mathcal{K}$  defined in Eq. (2.19) for Taylor states and in Eq. (2.26) for vacuum fields. To do this, we need to numerically apply the layer-potential operators  $\mathcal{S}_\lambda$ ,  $\partial_n \mathcal{S}_\lambda$  and  $\nabla \times \mathcal{S}_\lambda$ . These operators compute singular integrals on the boundary and therefore require special quadratures. We will discuss the details of their implementation in Section 3.2. In addition, for Taylor states, we also need to compute the surface vector field  $\mathbf{m}$ , as described in Eqs. (2.14, 2.15). This requires the discrete surface gradient operator  $\nabla_\Gamma$ , the inverse surface Laplacian  $\Delta_\Gamma^{-1}$  and the harmonic vector fields  $\{\mathbf{m}_H^1, \dots, \mathbf{m}_H^{N_s}\}$ . We will discuss the implementation of operators  $\nabla_\Gamma$  and  $\Delta_\Gamma^{-1}$  in Section 3.3 and the computation of harmonic vector fields in Section 3.4. Constructing the discrete operator  $\mathcal{K}$  from these building blocks is then straightforward.

To discretize the flux constraints in Eq. (2.23) and Eq. (2.27), we again need the layer-potential operators discussed above. The circulation integral is evaluated using a trapezoidal quadrature rule, which is spectrally accurate for this smooth periodic data.

### 3.1.4 Linear solver

After discretization, the linear system can be written in a block matrix form as,

$$\begin{bmatrix} \mathbf{A}_{11} & \mathbf{A}_{12} \\ \mathbf{A}_{21} & \mathbf{A}_{22} \end{bmatrix} \begin{bmatrix} \boldsymbol{\sigma} \\ \boldsymbol{\alpha} \end{bmatrix} = \begin{bmatrix} \mathbf{0} \\ \boldsymbol{\Phi} \end{bmatrix}, \quad (3.2)$$

where the first block-row corresponds to the boundary condition in Eq. (2.18) and the second block-row corresponds to the flux constraints in Eq. (2.23) for Taylor states; and likewise for the vacuum field formulation Eqs. (2.25, 2.27). Let  $N_s$  be the number of toroidal surfaces and  $N$  be the total number of surface discretization points. Then, the RHS boundary condition  $\mathbf{0}$  is a column vector of length  $N$  and the prescribed flux conditions  $\boldsymbol{\Phi}$  is a column vector of length  $N_s$ . Similarly, the unknown  $\boldsymbol{\sigma}$  is a column vector of length  $N$  and  $\boldsymbol{\alpha}$  is a column vector of length  $N_s$ .

For the problems considered in this work,  $N_s$  is small ( $N_s \leq 3$ ); however, the number of discretization points  $N$  can be as large as  $\mathcal{O}(1\text{E}+5)$ . It is computationally inefficient to directly construct the boundary integral operator  $\mathbf{A}_{11}$ , with dimensions  $N \times N$ , and it is instead implemented in a matrix-free form. Then, to solve Eq. (3.2), we first solve the following linear system for  $\mathbf{D}$ ,

$$\mathbf{A}_{11} \mathbf{D} = -\mathbf{A}_{12} \quad (3.3)$$

where  $\mathbf{D}$  is a matrix of size  $N \times N_s$ . We solve Eq. (3.3) using GMRES and this requires one solve for each of the  $N_s$  columns of  $\mathbf{D}$ . Then, we compute the unknowns  $\sigma$  and  $\alpha$  as follows,

$$\alpha = (\mathbf{A}_{21}\mathbf{D} + \mathbf{A}_{22})^{-1} \Phi, \quad (3.4)$$

$$\sigma = \mathbf{D}\alpha, \quad (3.5)$$

where the inverse of the  $N_s \times N_s$  matrix in Eq. (3.4) is computed directly.

### 3.1.5 Evaluating $B$

Once the unknowns  $\sigma$  and  $\alpha$  have been computed, we can evaluate the field  $B$  on the boundary  $\Gamma$  by discretizing and evaluating Eq. (2.17). This is analogous to the discretization of the boundary integral operator discussed above. To evaluate  $B$  at off-surface points, we discretize and evaluate the representation in Eq. (2.13). In our current implementation, we evaluate the layer-potentials at off-surface points using trapezoidal quadratures on an up-sampled mesh. If the off-surface points are close to the surface, then the upsample factor must be large and this scheme becomes very expensive. In the future, for such cases, we plan to use specialized quadratures for near-singular evaluation such as Quadrature by Expansion (QBX) [15, 37, 45].

## 3.2 High-order singular quadrature along surfaces

We now describe a quadrature rule to evaluate layer-potentials due to singular kernel functions. Our algorithm is adapted from the work of [5, 6] for the Helmholtz kernel and the work of [54] for the Stokes kernel. Fig. 3 gives a brief overview of the algorithm.

We consider a single toroidal surface  $\Gamma$ , parameterized by the toroidal and poloidal angles  $(\theta, \varphi) \in [0, 2\pi)^2$  and discretized on a uniform  $N_\theta \times N_\varphi$  grid as discussed in Section 3.1. The surface position is given by the function  $\mathbf{x}(\theta, \varphi)$ ; its discretization along the  $N$ -point grid is denoted by  $\mathbf{x}$ . And as before, given a function  $f(\theta, \varphi)$  along the grid, its discretization is denoted by  $\mathbf{f}$ . The layer-potential due to a kernel function  $\mathcal{G}$  at a target point  $\mathbf{x}_0 = \mathbf{x}(\theta_0, \varphi_0)$  on  $\Gamma$  is given by

$$\mathcal{G}[f](\mathbf{x}_0) = \int_{[0, 2\pi)^2} \mathcal{G}(\mathbf{x}_0 - \mathbf{x}(\theta, \varphi)) f(\theta, \varphi) \sqrt{\det \mathbf{G}(\theta, \varphi)} d\theta d\varphi \quad (3.6)$$

where  $\mathbf{G}$  is the metric tensor. The kernel function may be weakly-singular such as the single-layer Helmholtz kernel  $g_\lambda$  or of principal-value type such as the gradient of the single-layer Helmholtz kernel  $\nabla g_\lambda$ . To evaluate the layer-potential due to such kernels, we use a partition of unity to split the boundary integral into two integrals  $\mathcal{G}[f](\mathbf{x}_0) = U_G + U_L$  such that  $U_G$  is a smooth global integral over the entire surface and  $U_L$  is a singular local integral. We define  $U_G$  and  $U_L$  as

$$U_G = \int_{[0, 2\pi)^2} (1 - \eta(\theta, \varphi)) \mathcal{G}(\mathbf{x}_0 - \mathbf{x}) f(\theta, \varphi) \sqrt{\det \mathbf{G}} d\theta d\varphi \quad (3.7)$$

$$U_L = \int_{B_\eta} \eta(\theta, \varphi) \mathcal{G}(\mathbf{x}_0 - \mathbf{x}) f(\theta, \varphi) \sqrt{\det \mathbf{G}} d\theta d\varphi \quad (3.8)$$

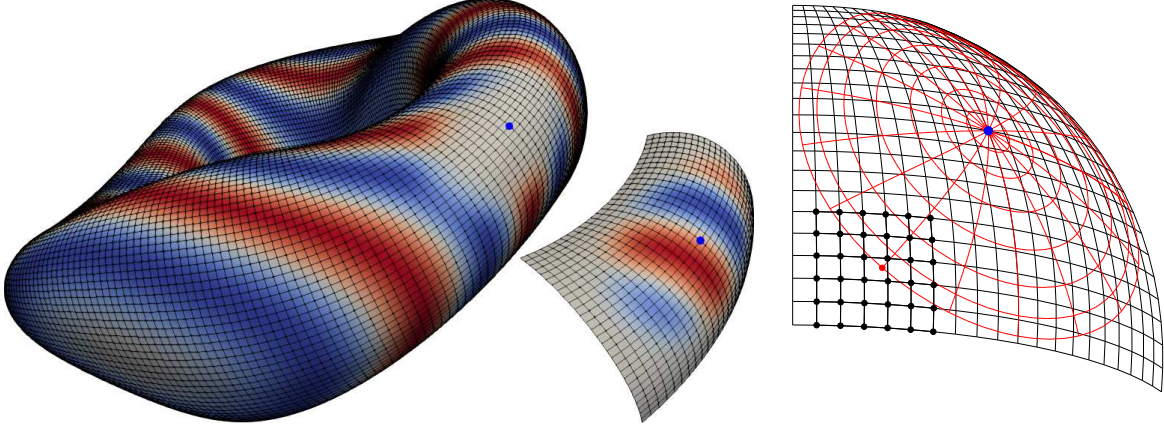


Figure 3: To evaluate the layer potential  $U = \mathcal{G}[f]$  at the blue target point on the surface, we use a partition of unity function  $\eta(\theta, \varphi)$  (centered at the target point) to separate the boundary integral into a smooth integral  $U_G = \mathcal{G}[(1 - \eta)f]$  over the entire surface and a singular integral  $U_L = \mathcal{G}[\eta f]$  over the support of  $\eta$ . We evaluate the smooth integral  $U_G$  using trapezoidal quadrature rule. We compute the singular integral  $U_L$  in polar coordinates using a trapezoidal rule in the angular direction and a Gauss-Legendre quadrature rule in the radial direction. The transformation from the regular grid discretization to a polar grid discretization is done using Lagrange interpolation on a  $12 \times 12$  grid.

where  $\eta(\theta, \varphi)$  is called a floating partition of unity centered at  $(\theta_0, \varphi_0)$  and  $B_\eta$  is the support of  $\eta$ . In order for the first integrand to be smooth and the second integrand to have compact support, we require that the function  $\eta$  be smooth, have compact support  $B_\eta$ , and that  $\eta(\theta, \varphi) = 1$  in a neighborhood around  $(\theta_0, \varphi_0)$ . To realize such a function, we define  $\eta$  as,

$$\eta(\theta, \varphi) = \chi \left( \frac{2}{M} \sqrt{\left( \frac{\theta - \theta_0}{h_\theta} \right)^2 + \left( \frac{\varphi - \varphi_0}{h_\varphi} \right)^2} \right) \quad (3.9)$$

where  $h_\theta = 2\pi/N_\theta$  and  $h_\varphi = 2\pi/N_\varphi$  are the discretization grid spacing in  $\theta$  and  $\varphi$ , respectively, and  $\chi : [0, \infty) \rightarrow [0, 1]$  is a smooth function such that  $\chi(\rho) = 1$  in a neighborhood of zero and  $\chi(\rho) = 0$  for  $\rho \geq 1$ . The parameter  $M$  is used to control the width of  $\eta$  so that its support  $B_\eta$  lies on an  $M \times M$  subset of the original  $N_\theta \times N_\varphi$  discretized grid. We will next discuss quadratures to numerically evaluate the smooth integral  $U_G$  and the singular integral  $U_L$ .

### 3.2.1 Quadrature for the smooth integrand

The integral in Eq. (3.7) is smooth, and we can therefore use standard quadratures for smooth functions to evaluate this integral with high accuracy. Since we already have a uniform discretization of periodic functions on an  $N_\theta \times N_\varphi$  grid, the trapezoidal rule is applicable and spectrally convergent:

$$U_G \approx \sum_{i,j} (1 - \eta_{ij}) \mathcal{G}_{ij} f_{ij} w_{ij} \quad (3.10)$$

where  $\eta_{ij} = \eta(\theta_i, \varphi_j)$ ,  $\mathcal{G}_{ij} = \mathcal{G}(\mathbf{x}_0 - \mathbf{x}_{ij})$  and  $w_{ij} = \frac{4\pi^2}{N_\theta N_\varphi} \sqrt{\det \mathbf{G}_{ij}}$  are the trapezoidal quadrature weights times the differential area element. When the discretization is suffi-

ciently fine to resolve the geometry, the area element  $\sqrt{\det \mathbf{G}}$  and the density  $f$ , the quadrature error is then determined by the smoothness of the term  $(1 - \eta) \mathcal{G}$ . This depends on how well the floating partition of unity  $\eta$  can be resolved on an  $M \times M$  grid of points and the effectiveness of  $(1 - \eta)$  at screening the kernel singularity. We will discuss the choice of  $\eta$  later in this section.

When computing the potential at all grid points, the summation in Eq. (3.10) requires  $\mathcal{O}(N^2)$  total cost for  $N$  grid points. This cost can be improved to  $\mathcal{O}(N)$  by using fast multipole method (FMM) acceleration [9, 22, 53]. However, we have not used FMM acceleration in the present work since the performance improvement would not be significant for the problem sizes considered here.

### 3.2.2 Quadrature for the singular integrand

Since the integral kernel  $\mathcal{G}$  has a singularity, we can not compute  $U_L$  directly using quadrature rules for smooth functions. To evaluate this integral, we apply a change of variables and compute the integral in polar coordinates. The coordinate transform removes the leading order kernel singularity allowing us to use standard quadratures and achieve high-order accuracy. In particular, we apply the following change of variables,

$$\theta = \theta_0 + (M/2)h_\theta \rho \sin \omega, \quad \text{and} \quad \varphi = \varphi_0 + (M/2)h_\varphi \rho \cos \omega,$$

where  $\rho$  and  $\omega$  are the radial and angular coordinate variables in the polar coordinate space and the pole is at the target  $\mathbf{x}_0$ . The boundary integral in Eq. (3.8) can then be written as,

$$U_L = \int_0^\pi \int_{-1}^1 \chi(\rho) \mathcal{G}(\mathbf{x}_0 - \mathbf{x}) f(\rho, \omega) \sqrt{\det \mathbf{G}} \frac{M^2 h_\theta h_\varphi}{4} |\rho| d\rho d\omega \quad (3.11)$$

where  $\frac{M^2 h_\theta h_\varphi}{4} |\rho|$  is the Jacobian of the transformation. For weakly-singular kernels (such as  $g_\lambda$ ) with  $1/|\mathbf{x}_0 - \mathbf{x}|$  singularity, the Jacobian cancels the singularity making the integrand bounded. In fact, in [5] it was shown that when the kernel  $\mathcal{G}$  is the real part of  $g_\lambda$ , then the integrand is smooth and periodic in  $\rho$ . This allowed them to use trapezoidal quadratures in both  $\rho$  and  $\omega$ . For integral operators such as  $\nabla_\Gamma \mathcal{S}_\lambda$ , the integrand in Eq. (3.11) is still singular and the integral must be understood in the Cauchy principal value sense. In [54], the authors showed that for the double-layer Stokes pressure kernel (a hypersingular kernel), the integral in  $\rho$  can be computed using a quadrature rule for smooth integrands if the quadrature is symmetric about the origin. The proof relies on showing that the integrand can be written as the sum of a smooth function and an antisymmetric singular function. The smooth integral can be computed using standard quadratures and the singular integral (which has zero principal value) evaluates to zero due to the symmetry of the quadrature rule. The same proof applies to many other kernels, including  $\nabla g_\lambda$ . For bounded kernel functions (such as the imaginary part of  $g_\lambda$ ), the integrand in Eq. (3.11) is only  $C^0$  continuous at the origin. To avoid having to deal with the real and the imaginary parts of  $g_\lambda$  separately, we compute the integral in  $\rho$  separately in each of the two intervals  $[-1, 0]$  and  $[0, 1]$  using a Gauss-Legendre quadrature rule. For the integral in  $\omega$ , we use trapezoidal quadrature rule.

To apply the quadrature in polar coordinates, we need to first evaluate the surface position  $\mathbf{x}$  and the density  $f$  at a new set of quadrature nodes. This requires interpolation from the uniform Cartesian grid discretization in  $\theta$  and  $\varphi$  to a polar grid discretization around

the target point. For each interpolation point in the polar grid, we select a  $12 \times 12$  array of values (surrounding the interpolation point) in the original discretization and use Lagrange interpolation to approximate the value at the interpolation point. Since we evaluate the polynomial interpolation close to the center of the interpolation grid, we do not suffer from Runge’s phenomenon and can use high-order interpolation. Using 12th order interpolation provides sufficient accuracy without being too expensive. We use  $\mathbf{R}$  to denote the interpolation operator that computes the polar grid discretization from the uniform discretization. Then, at the polar grid points, the surface position is given by  $\mathbf{x}^p = \mathbf{R}\mathbf{x}$  and the density is given by  $\mathbf{f}^p = \mathbf{R}\mathbf{f}$ . For the surface normal  $\mathbf{n}^p$  and the metric tensor  $\mathbf{G}^p$ , interpolating directly from values on the regular grid leads to poor accuracy. Instead, we first interpolate the tangent vectors  $\mathbf{x}_\theta^p = \mathbf{R}\mathbf{x}_\theta$  and  $\mathbf{x}_\varphi^p = \mathbf{R}\mathbf{x}_\varphi$ ; and then use these to compute  $\mathbf{n}^p$  and  $\mathbf{G}^p$  as was done in Eq. (3.1).

The polar grid quadrature nodes are given by a tensor-product rule with trapezoidal quadrature of order  $q$  in  $\omega$  and Gauss-Legendre quadrature of order  $q$  in  $\rho$  in the intervals  $[-1, 0]$  and  $[0, 1]$ . This gives us the quadrature nodes  $(\rho_i, \omega_i)$  and the quadrature weights  $w_i$  for  $i = 0, \dots, 2q^2 - 1$ . Once the values  $\mathbf{x}^p, \mathbf{n}^p$  and  $\mathbf{G}^p$  have been evaluated at the polar quadrature nodes through the interpolation process discussed above, we can apply the quadrature rule to approximate the integral in Eq. (3.11) as  $U_L \approx \mathbf{v}^T \mathbf{f}^p$  where for  $i = 0, \dots, 2q^2 - 1$ ,

$$v_i = \chi(\rho_i) \mathcal{G}(\mathbf{x}_0 - \mathbf{x}_i^p) \sqrt{\det \mathbf{G}_i} \frac{M^2 h_\theta h_\varphi}{4} |\rho_i| w_i.$$

Since the interpolation operator  $\mathbf{R}$  is a sparse matrix, for a given surface geometry we can easily precompute the quantity  $\mathbf{v}^T \mathbf{R}$  and then compute  $U_L \approx (\mathbf{v}^T \mathbf{R})\mathbf{f}$  several times for different densities  $\mathbf{f}$ . In the work of [5, 6] and [54], the interpolation was done by first upsampling the Cartesian discretization using FFT and then using low-order polynomial interpolation. While this may make the interpolation less expensive, it results in a dense interpolation operator and therefore makes the precomputation infeasible. Our scheme requires  $\mathcal{O}(q^2)$  cost per target for the precomputation and then the quadrature can be applied several times (with  $\mathcal{O}(M^2)$  cost per target) without the expensive kernel evaluations and interpolation of the density  $\mathbf{f}$  in each application. For a specified quadrature accuracy and a given surface, the optimal choice of the parameters  $M$  and  $q$  must be determined empirically. From [54], to obtain convergence as the mesh is refined, a good rule of thumb for scaling the parameters is given by  $M = \mathcal{O}(N^{1/4})$  and  $q = \mathcal{O}(N^{1/4})$ , where  $N = N_\theta N_\varphi$  is the number of surface mesh points. From the error analysis in [54], we expect spectral convergence with mesh refinement as we also appropriately scale the parameters  $M$  and  $q$ .

### 3.2.3 Partition of unity function

In Eq. (3.9), the floating partition of unity  $\eta$  is defined in terms of another function  $\chi$  that we define as:

$$\chi(\rho) = \exp(-36|\rho|^8). \quad (3.12)$$

Notice that  $\chi$  as defined above does not strictly satisfy the condition  $\chi(\rho) = 0$  for  $\rho \geq 0$ ; however, for computations in double-precision it is sufficiently small for  $\rho \geq 1$ . In Fig. 4, we compare  $\chi$  as defined here with the definition in [6]. We show  $\chi$  in the plot on the left and its periodic Fourier coefficients in the plot on the right. Comparing the two choices, we

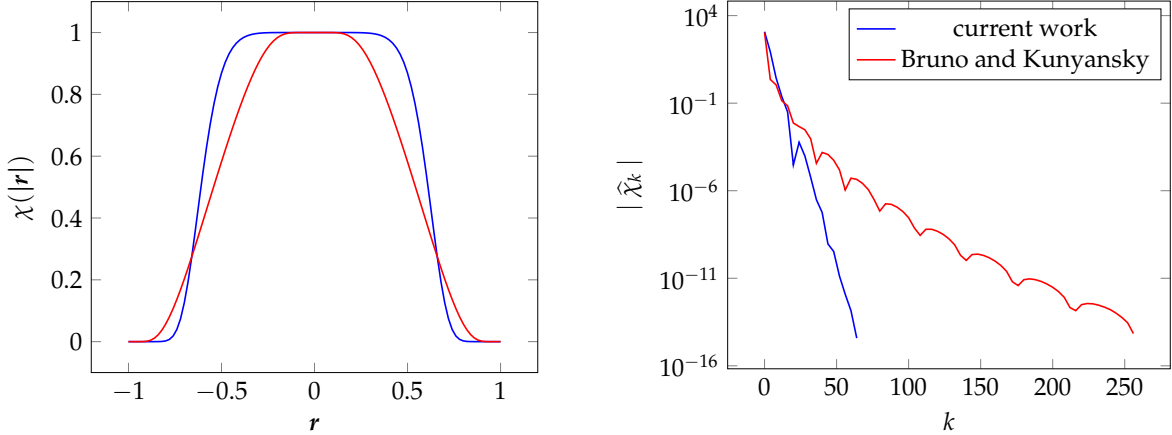


Figure 4: We compare the function  $\chi$  as defined in this work with the one used in [6]. The partition of unity function used in this work is close to 1 in a larger region around the origin, and is more effective in separating the singular and smooth parts of the kernel function. Furthermore, the periodic Fourier coefficients  $\hat{\chi}$  decay more rapidly, yielding a higher resolution splitting for the same number of grid points.

observe that our definition of  $\chi$  is close to 1 in a larger neighborhood around the origin and therefore, it is more effective at screening the kernel singularity in Eq. (3.7). We also note that the Fourier coefficients  $\hat{\chi}$  decay much more rapidly for our  $\chi$  and it therefore requires fewer grid points for the same resolution.

### 3.2.4 Performance optimizations

Kernel function evaluations for computing the smooth integrals is one of the most expensive parts of our quadrature scheme. For our application, we need to evaluate the potentials from the single-layer Helmholtz kernel function  $g_\lambda$  and its gradient  $\nabla g_\lambda$ . We have optimized kernel evaluations using shared-memory parallelism and through the use of AVX vector instructions for x86 processors. The inverse square root operation in the Laplace and the Helmholtz kernels is implemented using the fast approximate inverse square root instruction along with Newton iterations for additional accuracy as described in [42]. We use 13th order Taylor series approximation to evaluate  $\sin t$  to 12-digit accuracy in the interval  $[-\pi/4, \pi/4]$  and then evaluate  $\cos t = \sqrt{1 - \sin^2 t}$  using a procedure similar to the inverse square root operation. To evaluate  $\sin$  and  $\cos$  functions outside the range  $[-\pi/4, \pi/4]$ , we use rotations in the complex plane by multiplying with  $i = \sqrt{-1}$ . Our  $\sin$  and  $\cos$  evaluation algorithm performed slightly better than Intel’s SVML (Short Vector Math Library) in our experiments; however, we do not achieve full double-precision accuracy using 13th order Taylor series approximation. In Table 1, we present timing results to show the performance improvement achieved using these optimizations.

### 3.3 A spectral Laplace-Beltrami solver

Our spectral Laplace-Beltrami solver is based on previous work in [35, 43]. In [35], the surface Laplacian was implemented using Fourier pseudo-spectral differentiation and preconditioned using the exact inverse for the flat plane. The discrete Fourier transforms were

computed using FFTPACK [50] and the linear system was solved using BiCGSTAB. In our current work, we have improved performance by using the FFTW library [19] for computing the discrete Fourier transforms and using GMRES for the linear solve. A layer potential preconditioner for the Laplace-Beltrami equation was presented in [43] for high-order curvilinear triangular meshes. We have implemented this preconditioner using the quadratures discussed in Section 3.2. For completeness, we now briefly summarize the Laplace-Beltrami solver.

For a single toroidal surface  $\Gamma$ , the surface gradient, divergence and Laplace-Beltrami operators are given by,

$$\nabla_{\Gamma} f = [\mathbf{x}_{\theta} \ \mathbf{x}_{\varphi}] \mathbf{G}^{-1} \begin{bmatrix} \partial_{\theta} \\ \partial_{\varphi} \end{bmatrix} f, \quad (3.13)$$

$$\nabla_{\Gamma} \cdot \mathbf{v} = \frac{1}{\sqrt{|\mathbf{G}|}} [\partial_{\theta} \ \partial_{\varphi}] \sqrt{|\mathbf{G}|} \mathbf{v}, \quad (3.14)$$

$$\Delta_{\Gamma} f = \nabla_{\Gamma} \cdot \nabla_{\Gamma} f = \frac{1}{\sqrt{|\mathbf{G}|}} [\partial_{\theta} \ \partial_{\varphi}] \sqrt{|\mathbf{G}|} \mathbf{G}^{-1} \begin{bmatrix} \partial_{\theta} \\ \partial_{\varphi} \end{bmatrix} f, \quad (3.15)$$

where  $\mathbf{G}$  is the metric tensor,  $f$  is a scalar function on the surface and  $\mathbf{v}$  is a tangential vector field defined with respect to the tangent vectors  $\mathbf{x}_{\theta}$  and  $\mathbf{x}_{\varphi}$  such that  $\mathbf{v}(\theta, \varphi) = v_1(\theta, \varphi) \mathbf{x}_{\theta} + v_2(\theta, \varphi) \mathbf{x}_{\varphi}$ . The discrete surface gradient, divergence and Laplace-Beltrami operators are obtained by replacing  $\partial_{\theta}$  and  $\partial_{\varphi}$  with the discrete spectral differentiation operators  $\mathbf{D}_{\theta}$  and  $\mathbf{D}_{\varphi}$  respectively in Eqs. (3.13–3.15),

$$\nabla_{\Gamma_h} \mathbf{f} = [\mathbf{x}_{\theta} \ \mathbf{x}_{\varphi}] \mathbf{G}^{-1} \begin{bmatrix} \mathbf{D}_{\theta} \\ \mathbf{D}_{\varphi} \end{bmatrix} \mathbf{f}, \quad (3.16)$$

$$\nabla_{\Gamma_h} \cdot \mathbf{v} = \frac{1}{\sqrt{|\mathbf{G}|}} [\mathbf{D}_{\theta} \ \mathbf{D}_{\varphi}] \sqrt{|\mathbf{G}|} \mathbf{v}, \quad (3.17)$$

$$\Delta_{\Gamma_h} \mathbf{f} = \nabla_{\Gamma_h} \cdot \nabla_{\Gamma_h} \mathbf{f} = \frac{1}{\sqrt{|\mathbf{G}|}} [\mathbf{D}_{\theta} \ \mathbf{D}_{\varphi}] \sqrt{|\mathbf{G}|} \mathbf{G}^{-1} \begin{bmatrix} \mathbf{D}_{\theta} \\ \mathbf{D}_{\varphi} \end{bmatrix} \mathbf{f}, \quad (3.18)$$

where  $\mathbf{f}$ ,  $\mathbf{v}$  and  $\mathbf{G}$  are the discretizations of  $f$ ,  $\mathbf{v}$  and  $\mathbf{G}$  respectively. The Laplace-Beltrami operator has a nullspace of dimension one containing the space of constant functions. We use a rank-one update to make the operator full-rank and therefore uniquely invertible. The

Compiler	Laplace kernel		Helmholtz kernel	
	Un-vectorized	Vectorized	Un-vectorized	Vectorized
GCC-8.2	9.21	2.05	92.65	14.12
Intel-17.0.2	4.58	2.12	28.71	14.27

Table 1: Timing results in seconds on a single Intel Ivy Bridge CPU core (running at 2.5GHz) for  $1\text{E}+9$  kernel evaluations of the Laplace and the Helmholtz single-layer kernel functions compiled using GCC and Intel compilers, and comparing the un-vectorized and the vectorized implementations in each case. With GCC, we get  $4.5\times$  speedup for the Laplace kernel and  $6.5\times$  speedup for the Helmholtz kernel. The Intel compiler is able to auto-vectorize our un-vectorized code and therefore the speedups are not as large as with GCC; however, we still achieve over  $2\times$  speedup using explicit vectorization and our optimized implementation of sin and cos functions.

modified problem and the corresponding discrete problem are then given by:

$$\Delta_{\Gamma} u + \int_{\Gamma} u \, da = f \quad \text{and} \quad \Delta_{\Gamma_h} \mathbf{u} + \mathbf{w} \cdot \mathbf{u} = \mathbf{f}, \quad (3.19)$$

where  $f$  is the given RHS,  $u$  is the unknown,  $\mathbf{f}$  and  $\mathbf{u}$  are the discretizations of  $f$  and  $u$ , respectively, and  $w_{ij} = \frac{4\pi^2}{N_{\theta}N_{\varphi}} \sqrt{\det \mathbf{G}_{ij}}$  is the trapezoidal quadrature weight times the differential area element. We will next discuss two preconditioners for this problem. The final preconditioned problem is then solved using a GMRES code with modified Gram-Schmit orthogonalization from the PETSc library [1, 2].

### 3.3.1 Spectral preconditioner

In [35], the inverse of the Laplace-Beltrami operator for a flat surface was used to precondition Eq. (3.19). The pseudo-spectral inverse surface Laplacian can be constructed as follows,

$$\Delta_{I_h}^{-1} \mathbf{f} = \mathcal{F}^{-1} \mathbf{L} \mathcal{F} \mathbf{f} \quad (3.20)$$

where  $\mathbf{L}$  is a diagonal operator applied to the Fourier coefficients,

$$(\mathbf{L} \hat{\mathbf{f}})_{nm} = \begin{cases} 0, & \text{if } m = n = 0 \\ \left( \frac{n^2}{L_{\theta}^2} + \frac{m^2}{L_{\varphi}^2} \right)^{-1} \hat{f}_{nm}, & \text{otherwise.} \end{cases} \quad (3.21)$$

The parameters  $L_{\theta}$  and  $L_{\varphi}$  are the average surface lengths in the toroidal and poloidal direction respectively. They account for the anisotropy in the surface parameterization. The final preconditioned system is then obtained by left-preconditioning Eq. (3.19) with  $(\Delta_{I_h}^{-1} + \mathbf{1}\mathbf{1}^T)$  as follows,

$$\left( \Delta_{I_h}^{-1} + \mathbf{1}\mathbf{1}^T \right) \left( \Delta_{\Gamma_h} + \mathbf{1}\mathbf{w}^T \right) \mathbf{u} = \left( \Delta_{I_h}^{-1} + \mathbf{1}\mathbf{1}^T \right) \mathbf{f}, \quad (3.22)$$

where we have added  $\mathbf{1}\mathbf{1}^T$  to  $\Delta_{I_h}^{-1}$  to make it full rank.

### 3.3.2 Layer-potential preconditioner

In [43], it was shown that preconditioning Eq. (3.19) symmetrically with the Laplace single-layer potential operator  $\mathcal{S}_0$  results in a second-kind Fredholm equation. The preconditioned system is then given by:

$$\mathcal{S}_0 \left( \Delta_{\Gamma_h} + \mathbf{1}\mathbf{w}^T \right) \mathcal{S}_0 \mathbf{v} = \mathcal{S}_0 \mathbf{f}, \quad (3.23)$$

$$\mathbf{u} = \mathcal{S}_0 \mathbf{v}, \quad (3.24)$$

where we first solve Eq. (3.23) for  $\mathbf{v}$  using GMRES and then compute the final solution  $\mathbf{u}$  using Eq. (3.24).

In Section 4.2, we present results comparing the performance of these two preconditioners. While the spectral preconditioner is extremely efficient to compute due to the use of FFT, it can only be applied to uniform surface discretizations. On adaptive meshes, the inverse of the 2D Laplacian can be applied using a specialized fast multipole method [18] or

other fast Poisson solvers; however, this is not straightforward. In addition, it is sensitive to the surface parameterization. On the other hand, the layer-potential preconditioner is not sensitive to the surface parameterization provided the surface quadratures are computed accurately. It can also be applied to adaptive meshes, provided appropriate quadratures are available to compute the layer-potentials. However, despite the performance optimizations discussed in Section 3.2, the surface quadratures can still be expensive to compute. For our current application, the spectral preconditioner is both fast and sufficiently robust.

### 3.4 Computing harmonic vector fields

On general smooth closed surfaces, harmonic vector fields are not known analytically and must be solved for. Only in specialized geometries, e.g. surfaces of revolution, do formulae exist [8, 14]. Recall that a harmonic vector field  $\mathbf{m}_H$  is one such that  $\nabla_\Gamma \cdot \mathbf{m}_H = 0$  and  $\nabla_\Gamma \cdot \mathbf{n} \times \mathbf{m}_H = 0$ . In our case, when computing Taylor states using the generalized Debye representation, we need to compute a basis for harmonic vector fields subject to an additional constraint, namely that  $\mathbf{n} \times \mathbf{m}_H = -i\mathbf{m}_H$ . Such harmonic vector fields  $\mathbf{m}_H$  can be computed for each toroidal surface and are unique up to a complex scaling factor. We follow the scheme described in [43] and start with a smooth tangential vector field  $\mathbf{v}$ . In our implementation, we choose  $\mathbf{v} = \mathbf{x}_\theta$ . We first compute the non-harmonic terms of its Hodge decomposition,

$$\mathbf{v} = \nabla_\Gamma \alpha + \mathbf{n} \times \nabla_\Gamma \beta + \mathbf{v}_H,$$

where  $\alpha$  and  $\beta$  are unknown scalar functions obtained by solving the following two Laplace-Beltrami problems:

$$\Delta_\Gamma \alpha = \nabla_\Gamma \cdot \mathbf{v}, \quad \text{and} \quad \Delta_\Gamma \beta = -\nabla_\Gamma \cdot \mathbf{n} \times \mathbf{v}.$$

Then, we can compute  $\mathbf{v}_H = \mathbf{v} - \nabla_\Gamma \alpha - \mathbf{n} \times \nabla_\Gamma \beta$  and finally obtain the required harmonic vector field as  $\mathbf{m}_H = \mathbf{v}_H + i\mathbf{n} \times \mathbf{v}_H$ .

### 3.5 Algorithm summary

In this section, we discussed the discretization of the boundary data on a uniform spectral mesh. We have presented a quadrature scheme which is used to compute boundary convolutions with the kernels  $g_\lambda(\mathbf{r})$  and  $\nabla g_\lambda(\mathbf{r})$ . These schemes are used to construct the discretized convolution operators  $\mathcal{S}_\lambda, \nabla \mathcal{S}_\lambda$ . The operator  $\nabla \times \mathcal{S}_\lambda$  can similarly be constructed from the result of  $\nabla \mathcal{S}_\lambda$ . We discussed a spectral Laplace-Beltrami solver along with two efficient preconditioners, and showed how to compute harmonic vector fields using the Laplace-Beltrami solver. The harmonic vector fields are then used to discretize our boundary integral operator  $\mathcal{K}$  in Eq. (2.18). The resulting system is then solved as described in Section 3.1. This requires  $N_s$  solves of the boundary integral operator using GMRES. We summarize the total cost of different stages of our algorithm for computing Taylor states in Table 2. Since our quadrature scheme and the Laplace-Beltrami solver are both spectrally accurate with mesh refinement, we expect to see spectral convergence for the overall solver as well. In the next section, we present empirical numerical results to show convergence and solve times for different stages of our solver.

	$T_{setup} =$		$Nq^2$
Layer potential quadrature	$T_{smooth} =$	$N_s N_{GMRES}$	$\times N^2$
	$T_{singular} =$	$N_s N_{GMRES}$	$\times NM^2$
	$T_{quad-eval} =$	$T_{smooth} + T_{singular}$	
Spectral Laplace-Beltrami	$T_{LB} =$	$N_s N_{GMRES} N_{LB}$	$\times N \log N$

Table 2: Cost complexity for different stages of the algorithm for  $N_s$  surfaces with  $N$  total surface discretization points,  $N_{GMRES}$  GMRES iterations for each Boundary Integral Equation (BIE) solve, and  $N_{LB}$  iterations for each Laplace-Beltrami solve.  $T_{LB}$  is the total cost for  $N_s N_{GMRES}$  Laplace-Beltrami solves using the spectral preconditioner. The setup cost for the quadratures is  $T_{setup}$ , and the total cost of quadrature evaluation  $T_{quad-eval}$  is the sum of cost of the singular correction  $T_{singular}$  and the cost of the smooth quadrature  $T_{smooth}$ .

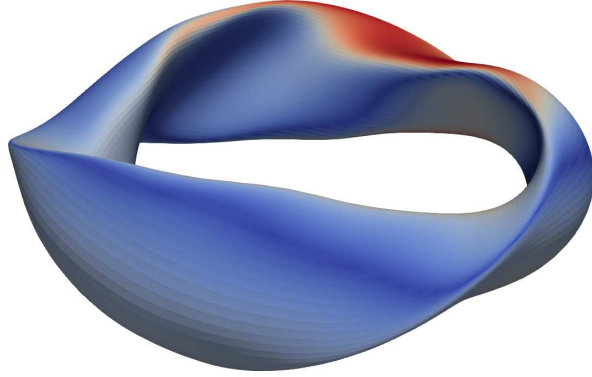


Figure 5: The surface and the magnitude of the reference potential  $u$  for the convergence results presented in Table 3. The surface is the outer surface of the QAS3 stellarator [20]. The reference potential is generated by a single point source outside the bounded domain  $\Omega$ .

## 4 Numerical experiments

We now present numerical results to demonstrate convergence and efficiency of the quadrature scheme for singular integrands detailed in Section 4.1, the spectral Laplace-Beltrami solver in Section 4.2, and the full solver for computing Taylor states in Section 4.3. All numerical errors reported in this section are relative errors. Our experiments were performed on a Linux workstation with quad 15-core Intel Xeon E7-4880 v2 CPUs running at 2.5GHz with 1.5TB of RAM. We use Intel compiler version 17.0.2 with O3 optimization level and AVX vectorization enabled.

### 4.1 Singular quadrature

In this section, we present convergence results for our singular surface quadrature scheme. We use Green's third identity to verify and evaluate the accuracy of our method. For a solution  $u$  to the homogeneous Helmholtz equation in a bounded domain  $\Omega \subset \mathbb{R}^3$ , Green's

identity states that,

$$u(\mathbf{x}) = \int_{\Gamma} g_{\lambda}(\mathbf{x} - \mathbf{y}) \partial_{n_y} u(\mathbf{y}) \, da_y - \int_{\Gamma} u(\mathbf{y}) \partial_{n_y} g_{\lambda}(\mathbf{x} - \mathbf{y}) \, da_y, \quad \text{for } \mathbf{x} \in \Omega.$$

Taking the limit as  $\mathbf{x} \rightarrow \Gamma$ , with  $\mathbf{x} \in \Omega$ , along the boundary  $\Gamma$  we have

$$u(\mathbf{x}) = \frac{u}{2}(\mathbf{x}) + \mathcal{S}_{\lambda}[\partial_n u](\mathbf{x}) - \mathcal{D}_{\lambda}[u](\mathbf{x}), \quad \text{for } \mathbf{x} \in \Gamma \quad (4.1)$$

where  $\mathcal{S}_{\lambda}[\cdot]$  and  $\mathcal{D}_{\lambda}[\cdot]$  are the single- and double-layer potential operators on  $\Gamma$  which compute convolutions with  $g_{\lambda}$  and  $\partial_n g_{\lambda}$  respectively. We compute the RHS in Eq. (4.1) using our quadrature scheme and compare it to the reference potential  $u$  on  $\Gamma$ . The reference potential  $u$  is generated using a single source  $\mathbf{x}_0$  outside of the domain  $\Omega$ ; i.e.  $u(\mathbf{x}) = g_{\lambda}(\mathbf{x} - \mathbf{x}_0)$ .

The surface geometry and the magnitude of the reference potential  $u$  in our experiments are visualized in Fig. 5. The geometry corresponds to the QAS3 stellarator proposed by Paul Garabedian, whose outer surface can be constructed from the coefficients given in Table II of reference [20]. We present convergence results for  $\lambda = 0$  and  $\lambda = 1$  in Table 3. For both sets of results, we show convergence to about 8-digits in  $L^{\infty}$ -norm as we refine the mesh from  $N = 70 \times 14$  unknowns to  $N = 700 \times 140$  unknowns, increase the dimension  $M$  of the square partition-of-unity patch, and increase the order  $q$  of the polar quadrature. In each case, we have selected the optimal values of the parameters  $N$ ,  $M$  and  $q$  to minimize the computation time for a given accuracy. As expected from the error analysis, we observe spectral convergence in each case.

In Table 3, we also report a breakdown of the total time into the setup time  $T_{\text{setup}}$  and the evaluation time  $T_{\text{quad-eval}} = T_{\text{singular}} + T_{\text{smooth}}$  on 1-CPU core and 60-CPU cores. The setup stage is required only once for a fixed geometry shape; therefore, when solving boundary integral equations using iterative linear solvers, the setup cost is amortized. As we increase the problem size, the setup time  $T_{\text{setup}}$  scales as  $\mathcal{O}(Nq^2)$ . For the evaluation phase  $T_{\text{quad-eval}}$ , the  $\mathcal{O}(N^2)$  complexity of the N-body computation is the dominant cost and the  $\mathcal{O}(NM^2)$  cost of singular correction accounts for only a small fraction of the evaluation time. Comparing the timings for 1-CPU core and 60-CPU cores, we observe that both the setup and evaluation stages scale well for sufficiently large problems, with parallel efficiency up to 90%. Notice that the evaluation time for  $\lambda = 0$  is much smaller than for  $\lambda = 1$ ; this is because the former uses the Laplace single-layer and double-layer kernel functions, which do not require expensive sin and cos function evaluations.

## 4.2 Laplace-Beltrami solver

We now show convergence results for our spectral Laplace-Beltrami solver. In the following experiments, we solve  $\Delta_{\Gamma} \varphi = f$  on  $\Gamma$ . We define the function  $f$  in terms of a 3D harmonic potential  $u$  as follows,

$$f = \Delta_{\Gamma} u|_{\Gamma} = -2H \frac{\partial u}{\partial \mathbf{n}} - \frac{\partial^2 u}{\partial \mathbf{n}^2}$$

where  $H$  is the mean curvature function over  $\Gamma$ . Then, the exact solution  $\varphi$  is given by projecting  $u$  to the space of mean-zero functions on  $\Gamma$ ,

$$\varphi = u|_{\Gamma} - \frac{1}{|\Gamma|} \int_{\Gamma} u \, da$$

where  $|Γ|$  is the surface area of  $Γ$ . In our experiments, we choose  $u$  to be the Coulombic potential from a single off-surface point charge. The boundary geometry  $Γ$  along with reference solution  $φ$  and the RHS  $f$  are visualized in Fig. 6. For this test, we also took  $Γ$  to be the outer surface of the QAS3 stellarator [20].

In Table 4, we present convergence results using the two preconditioners discussed in Section 3.3. In the spectral preconditioner case, we use left preconditioning with the exact  $Δ_T^{-1}$  operator for the flat plane. In the layer-potential preconditioner case, we use symmetric preconditioning with the single-layer potential operator associated with the Laplace’s equation. Without preconditioning, the solver did not converge to the desired accuracy within 300 GMRES iterations and therefore we have omitted those results. The results show convergence in the relative  $L^\infty$ -norm of the error as we refine the mesh from  $N = 70 \times 14$  unknowns to  $N = 700 \times 140$  unknowns and reduce the GMRES tolerance  $\epsilon_{\text{GMRES}}$ . The relative error  $\|e\|_\infty$  (compared to the reference solution) converges spectrally to about 8-digits for both preconditioners. The number of GMRES iterations  $N_{LB}$  grows only modestly with the desired precision. We also report the solve time  $T_{p=1}$  on 1-CPU core and  $T_{p=60}$  on 60-CPU cores. From the solve times  $T_{p=1}$ , we observe that the solves using the spectral preconditioner scale as expected with a cost of  $\mathcal{O}(N_{LB}N \log N)$ . Similarly, the solves with the layer-potential preconditioner scale as  $\mathcal{O}(N_{LB}N^2)$ . This cost can be reduced to  $\mathcal{O}(N_{LB}N)$  by accelerating using the fast multipole method (FMM); however, depending on the specific FMM implementation and desired precision, this would only be advantageous for large problems ( $N > 20K$ ). Comparing  $T_{p=1}$  and  $T_{p=60}$ , we observe that for the spectral preconditioner, the solve time does not improve from using multiple CPU-cores since the FFT is a memory bound operation. For the layer-potential preconditioner, we observe up to  $48\times$  speedup for the largest problem on 60-CPU cores since the quadrature evaluation is compute bound. Comparing the two preconditioners, the layer-potential potential is more effective in reducing the number of GMRES iterations  $N_{LB}$ ; however, it is still much more ex-

$\lambda$	$N$	$M$	$q$	$\ e\ _\infty$	1-core			60-cores		
					$T_{\text{setup}}$	$T_{\text{singular}}$	$T_{\text{smooth}}$	$T_{\text{setup}}$	$T_{\text{singular}}$	$T_{\text{smooth}}$
0.0	9.8E+2	12	15	2.0E-3	0.7	0.001	0.006	0.03	0.001	0.003
	3.9E+3	24	24	3.9E-5	6.9	0.02	0.09	0.16	0.002	0.01
	1.6E+4	30	30	1.2E-6	42.9	0.09	1.3	0.9	0.008	0.09
	4.8E+4	40	36	4.3E-8	190.8	0.5	12.2	3.6	0.02	0.34
	9.8E+4	50	42	3.3E-9	543.5	1.4	50.5	10.3	0.07	1.14
1.0	9.8E+2	12	15	2.6E-3	1.1	0.004	0.03	0.04	0.002	0.003
	3.9E+3	24	24	1.5E-4	11.9	0.04	0.6	0.26	0.005	0.02
	1.6E+4	30	30	4.0E-6	74.9	0.3	8.7	1.4	0.02	0.19
	4.8E+4	40	36	1.1E-7	337.8	1.3	80.7	6.1	0.05	1.53
	9.8E+4	50	42	7.2E-9	946.7	4.0	334.9	17.5	0.17	6.14

Table 3: Convergence results for the singular quadrature scheme for the Laplace kernel  $\lambda = 0$  and the Helmholtz kernel  $\lambda = 1$ . Fig. 5 shows the surface and the reference solution used in these experiments. We show convergence in the relative  $L^\infty$ -norm of the error as we refine the mesh  $N$ , increase the dimension of the partition-of-unity patch  $M$  and increase the order of the polar-quadrature  $q$ . We also report the setup time  $T_{\text{setup}}$  and a breakdown of the evaluation time  $T_{\text{quad-eval}} = T_{\text{singular}} + T_{\text{smooth}}$ . To show scalability of our code, we present timing results on 1-CPU core and on 60-CPU cores.

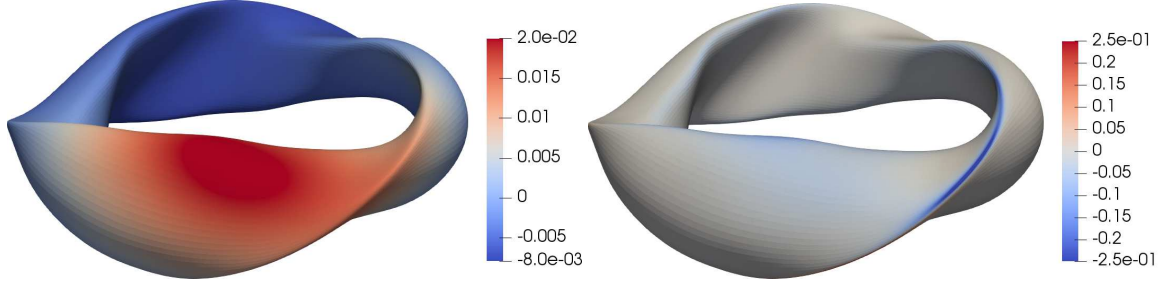


Figure 6: The surface geometry with the reference solution  $\varphi$  (left) and the input  $f$  (right) to the Laplace-Beltrami solver for the convergence results in Table 4. The surface is the outer surface of the QAS3 stellarator [20].

pensive due to the high cost of the quadratures. Since the layer-potential preconditioner has better parallel scalability, in parallel the timings for the two schemes become comparable.

### 4.3 Computing Taylor states

We now present numerical results to show convergence of our boundary integral solver for Taylor states. In [8], a method for constructing analytic solutions for Taylor states in axisymmetric geometries was discussed and we used this to construct reference solutions for testing our numerical scheme in [44]. We are not aware of a general method for generating analytic solutions for non-axisymmetric geometries. Therefore, to evaluate the accuracy of our solver, we instead solve a related boundary value problem discussed below.

We construct a reference Taylor state  $B_0$  given by,

$$B_0 = \lambda Q_0 + \nabla \times Q_0, \quad (4.2)$$

$$Q_0(x) = \oint_C g_\lambda(x, y) m_0 dl(y),$$

where  $m_0$  is a constant generalized Debye current in a loop  $C$  around the domain  $\Omega$ . The generalized Debye current loop is shown in red in Fig. 7. By construction,  $B_0$  satisfies  $\nabla \times B_0 = \lambda B_0$ ; however, in general, it does not satisfy the boundary condition  $B_0 \cdot n = 0$  on  $\Gamma$ .

$N$	spectral preconditioner					layer-potential preconditioner				
	$\epsilon_{\text{GMRES}}$	$N_{LB}$	$\ e\ _\infty$	$T_{p=1}$	$T_{p=60}$	$\epsilon_{\text{GMRES}}$	$N_{LB}$	$\ e\ _\infty$	$T_{p=1}$	$T_{p=60}$
3.9E+3	3.5E-3	7	1.9E-2	0.010	0.022	8.8E-2	3	1.4E-1	0.30	0.018
8.8E+3	5.2E-4	11	2.8E-3	0.029	0.050	1.3E-2	6	7.2E-3	2.59	0.086
1.6E+4	6.0E-5	16	4.6E-4	0.07	0.10	1.5E-3	7	1.3E-3	8.89	0.28
3.5E+4	2.1E-6	24	2.0E-5	0.26	0.37	5.1E-5	10	1.6E-5	60	1.39
6.3E+4	8.5E-8	32	1.1E-6	0.63	0.78	2.1E-6	12	8.0E-7	222	4.76
9.8E+4	9.8E-9	37	9.1E-8	1.35	1.42	2.4E-7	13	6.3E-8	576	11.9

Table 4: Convergence results for the Laplace-Beltrami solver for the problem shown in Fig. 6, using the spectral preconditioner and the layer-potential preconditioner. We show convergence in the relative  $L^\infty$  norm of the error  $\|e\|_\infty$  as we increase the number of discretization grid points  $N$ , and reduce the GMRES tolerance  $\epsilon_{\text{GMRES}}$ . We also report the number of GMRES iterations  $N_{LB}$  and the solve time  $T_{p=1}$  on 1-CPU core and  $T_{p=60}$  on 60-CPU cores (not including the setup time for quadratures).

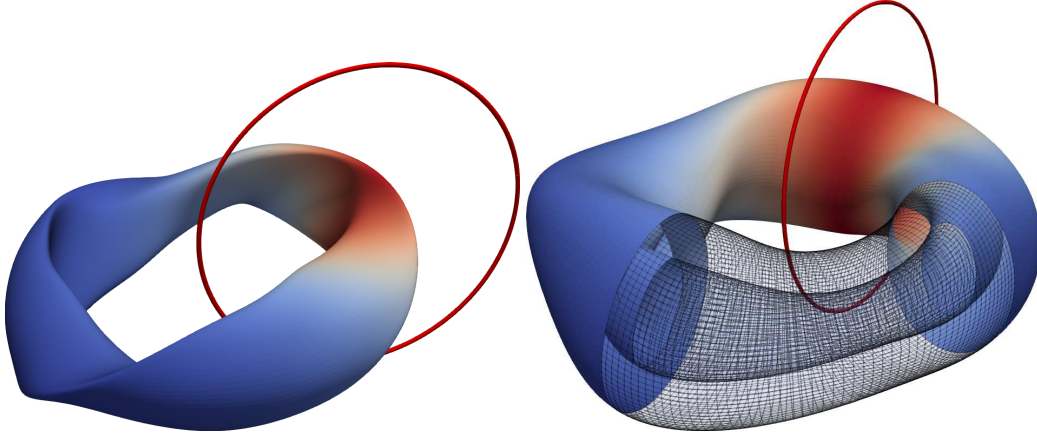


Figure 7: Taylor states in toroidal (left) and toroidal-shell (right) domains. The first shape is the outer surface of the QAS3 stellarator [20]. In the second geometry, each surface is the surface of revolution a rotating ellipse as described in Section 4.3.2. The reference solution  $\mathbf{B}_0$  visualized here is generated by a generalized Debye current loop (shown in red) around the domain. Convergence results for these geometries are presented in Tables 5 and 6.

Therefore, instead of solving the original problem in Eq. (2.11), we solve the following more general problem where  $\mathbf{B} \cdot \mathbf{n}$  on the boundary is non-zero,

$$\begin{aligned} \nabla \times \mathbf{B} &= \lambda \mathbf{B}, & \text{in } \Omega, \\ \mathbf{B} \cdot \mathbf{n} &= \mathbf{B}_0 \cdot \mathbf{n}, & \text{on } \Gamma, \end{aligned} \quad (4.3)$$

while also matching the appropriate flux conditions (or equivalently the circulation as discussed in Section 2.2) for  $\mathbf{B}$  and  $\mathbf{B}_0$ . Due to uniqueness, the numerically computed solution  $\mathbf{B}$  should match the reference solution  $\mathbf{B}_0$  at all points in the interior of the domain  $\Omega$ . Below, we test our solver for the two domains shown in Fig. 7.

#### 4.3.1 Toroidal domain

The domain along with the magnitude of the reference solution  $\mathbf{B}_0$  are visualized on the left in Fig. 7. Once more, the surface is the outer surface of the QAS3 stellarator [20]. We discretize the current loop (shown in red) using  $1\text{E}+3$  equispaced points and compute the line integral in Eq. (4.2) using trapezoidal quadrature rule. Since the domain  $\Omega$  and the current loop  $C$  are sufficiently separated, the reference solution  $\mathbf{B}_0$  computed in this way is accurate to 16-digits at points on  $\Omega$ . We evaluate  $\mathbf{B}_0 \cdot \mathbf{n}$  on  $\Gamma$  and the toroidal flux  $\Phi_{\mathbf{B}_0}^{\text{tor}}$  in a cross section of  $\Omega$ . Then, we setup the following discretized linear system,

$$\begin{bmatrix} \mathbf{A} & \mathbf{u}_1 \\ \mathbf{v}_1^T & c_{11} \end{bmatrix} \begin{bmatrix} \sigma \\ \alpha \end{bmatrix} = \begin{bmatrix} \mathbf{B}_0 \cdot \mathbf{n} \\ \Phi_{\mathbf{B}_0}^{\text{tor}} \end{bmatrix}.$$

We solve this block linear system with a procedure similar to the one described before in Eqs. (3.3–3.5), except that the  $\mathbf{B}_0 \cdot \mathbf{n}$  is non-zero. The unknowns  $\sigma$  and  $\alpha$  are given by

$$\begin{aligned} \alpha &= (\mathbf{v}_1^T \mathbf{d} + c)^{-1} (\Phi_{\mathbf{B}_0}^{\text{tor}} - \mathbf{v}_1^T \mathbf{w}) \\ \sigma &= \mathbf{w} - \mathbf{d}\alpha \end{aligned}$$

$\lambda$	$N$	$\epsilon_{\text{GMRES}}$	$(N_s + 1) N_{\text{GMRES}}$	$\ e\ _\infty$	$T_{\text{setup}}$	$T_{LB}$	$T_{\text{quad-eval}}$	$T_{\text{solve}}$
0.5	8.8E+3	9.6E-3	24	2.6E-2	1.6	8.2	4.4	14.3
	2.5E+4	6.5E-4	33	2.2E-3	7.0	39.4	36.9	83.2
	4.8E+4	1.5E-4	38	3.8E-4	15.8	101.4	143.9	261.0
	7.9E+4	1.5E-5	43	4.9E-5	31.7	256.9	434.2	722.7
	9.8E+4	3.6E-6	46	2.2E-5	44.7	342.9	693.8	1081.4
	2.2E+5	6.8E-8	56	5.3E-7	148.1	1314.8	4074.9	5537.8
	3.9E+5	4.0E-9	61	3.1E-8	366.2	2803.7	13718.0	16889.0
	6.1E+5	1.0E-9	66	4.4E-9	704.9	6242.9	35729.0	42676.5
1.0	8.8E+3	9.6E-3	34	3.3E-2	1.6	11.0	5.9	18.5
	2.5E+4	6.5E-4	45	2.5E-3	6.8	53.2	48.9	109.0
	4.8E+4	1.5E-4	50	4.3E-4	15.7	135.5	184.5	335.7
	7.9E+4	1.5E-5	58	6.2E-5	31.6	355.4	568.3	955.3
	9.8E+4	3.6E-6	63	2.3E-5	44.1	478.7	921.3	1444.0
	2.2E+5	6.8E-8	78	5.5E-7	148.1	1861.1	5545.8	7555.0
	3.9E+5	4.0E-9	85	2.9E-8	366.2	3894.2	18597.0	22857.4
	6.1E+5	1.0E-9	88	6.5E-9	704.9	8381.8	46458.0	55544.7

Table 5: Convergence results for the geometry and reference solution in Fig. 7 (left). We present results for two different values of the Beltrami parameter  $\lambda = 0.5$  and  $\lambda = 1$ . We observe spectral convergence in the error  $\|e\|_\infty$  with increasing mesh-refinement  $N$  as we also reduce the GMRES tolerance  $\epsilon_{\text{GMRES}}$  and correspondingly increase the quadrature accuracy (using parameters  $M$  and  $q$ ). We also report the total number of GMRES iterations  $(N_s + 1) N_{\text{GMRES}}$  and the breakdown of the total solve time  $T_{\text{solve}} \approx T_{\text{setup}} + T_{LB} + T_{\text{quad-eval}}$  on 60-CPU cores.

where  $w = \mathbf{A}^{-1} \mathbf{B}_0 \cdot \mathbf{n}$  and  $\mathbf{d} = \mathbf{A}^{-1} \mathbf{u}_1$ . The operator  $\mathbf{A}^{-1}$  must be applied twice and this is accomplished using two GMRES solves. Next, using  $\sigma$  and  $\alpha$ , we evaluate  $\mathbf{B}$  at points in the interior of  $\Omega$  and compare with the reference solution  $\mathbf{B}_0$ .

In Table 5, we report the maximum relative error  $\|e\|_\infty = \|\mathbf{B} - \mathbf{B}_0\|_\infty / \|\mathbf{B}_0\|_\infty$  in  $\Omega$  for two sets of experiments with  $\lambda = 0.5$  and  $\lambda = 1$  respectively. In each case, we show convergence as we reduce the GMRES tolerance  $\epsilon_{\text{GMRES}}$ , increase the mesh refinement  $N$ , and correspondingly increase the quadrature accuracy. In both sets of results, we observe spectral convergence to about 5-digits of accuracy. We also report the total number of GMRES iterations  $(N_s + 1) N_{\text{GMRES}}$  and the total solve time  $T_{\text{solve}}$  on 60-CPU cores. We observe that problems with larger  $\lambda$  require a larger number of GMRES iterations and proportionally longer solve times. This is well-known in wave propagation problems, and can be attributed to the spectrum of the boundary integral operator  $\mathbf{A}$  slightly de-clustering as  $\lambda$  increases.

### 4.3.2 Toroidal-shell domain

We now present convergence results for the geometry on the right in Fig. 7. The domain  $\Omega$  is the region between the two toroidal surfaces, each of which is the surface of revolution of a rotating ellipse described by the following equation in cylindrical coordinates,

$$\begin{bmatrix} R(\theta, \varphi) \\ Z(\theta, \varphi) \end{bmatrix} = \begin{bmatrix} R_0 \\ 0 \end{bmatrix} + \begin{bmatrix} \cos \frac{3}{2}\theta & -\sin \frac{3}{2}\theta \\ \sin \frac{3}{2}\theta & \cos \frac{3}{2}\theta \end{bmatrix} \begin{bmatrix} a & 0 \\ 0 & b \end{bmatrix} \begin{bmatrix} \cos \frac{3}{2}\theta & \sin \frac{3}{2}\theta \\ -\sin \frac{3}{2}\theta & \cos \frac{3}{2}\theta \end{bmatrix} \begin{bmatrix} \cos \varphi \\ \sin \varphi \end{bmatrix}. \quad (4.4)$$

The outer surface is described by Eq. (4.4) with  $R_0 = 2.0$ ,  $a = 0.7$  and  $b = 1.0$ . Similarly, the inner surface is described by Eq. (4.4) with  $R_0 = 2.0$ ,  $a = 0.3$  and  $b = 0.55$ . As in the previous case, the reference solution  $\mathbf{B}_0$  is generated by a generalized Debye current loop around the  $\Omega$  and is evaluated using Eq. (4.2) and trapezoidal quadrature rule. We evaluate  $\mathbf{B}_0 \cdot \mathbf{n}$  on the domain boundary  $\Gamma$ . In this setup, we require two flux constraints; the toroidal flux  $\Phi_{\mathbf{B}_0}^{tor}$  and the poloidal flux  $\Phi_{\mathbf{B}_0}^{pol}$ . We setup the discretized boundary integral problem for the solution  $\mathbf{B}$  in the following block form,

$$\begin{bmatrix} \mathbf{A} & \mathbf{u}_1 & \mathbf{u}_2 \\ \mathbf{v}_1^T & c_{11} & c_{12} \\ \mathbf{v}_2^T & c_{21} & c_{22} \end{bmatrix} \begin{bmatrix} \sigma \\ \alpha \\ \beta \end{bmatrix} = \begin{bmatrix} \mathbf{B}_0 \cdot \mathbf{n} \\ \Phi_{\mathbf{B}_0}^{tor} \\ \Phi_{\mathbf{B}_0}^{pol} \end{bmatrix}.$$

We then solve this linear system for the unknowns  $\sigma$  and  $\varphi$  as follows,

$$\begin{bmatrix} \alpha \\ \beta \end{bmatrix} = \left( \begin{bmatrix} \mathbf{v}_1^T \\ \mathbf{v}_2^T \end{bmatrix} \begin{bmatrix} \mathbf{d}_1 & \mathbf{d}_2 \end{bmatrix} + \begin{bmatrix} c_{11} & c_{12} \\ c_{21} & c_{22} \end{bmatrix} \right)^{-1} \left( \begin{bmatrix} \Phi_{\mathbf{B}_0}^{tor} \\ \Phi_{\mathbf{B}_0}^{pol} \end{bmatrix} - \begin{bmatrix} \mathbf{v}_1^T \\ \mathbf{v}_2^T \end{bmatrix} \mathbf{w} \right)$$

$$\sigma = \mathbf{w} - \begin{bmatrix} \mathbf{d}_1 & \mathbf{d}_2 \end{bmatrix} \begin{bmatrix} \alpha \\ \beta \end{bmatrix}$$

where  $\mathbf{w} = \mathbf{A}^{-1} \mathbf{B}_0 \cdot \mathbf{n}$  and  $\begin{bmatrix} \mathbf{d}_1 & \mathbf{d}_2 \end{bmatrix} = \mathbf{A}^{-1} \begin{bmatrix} \mathbf{u}_1 & \mathbf{u}_2 \end{bmatrix}$ . The numerical results in Table 6 show convergence in  $\|e\|_\infty$  to about 8-digits as we decrease the GMRES tolerance  $\epsilon_{\text{GMRES}}$  and increase the mesh refinement  $N$ . We also report the total number of GMRES iterations  $(N_s + 1) N_{\text{GMRES}}$  and the total solve time  $T_{\text{solve}}$  on 60-CPU cores.

#### 4.4 Comparison with SPEC

In Table 7, we compare our solver with the SPEC code of [40]. We present results for the geometry corresponding to the plasma boundary in the Wendelstein 7-X (W7-X) stellarator [4, 48]. We constructed reference solutions for  $\lambda = 0$  and  $\lambda = 1$  with our BIE code using very fine discretization ( $N = 8.2\text{E}+5$ ,  $\epsilon_{\text{GMRES}} = 1\text{E}-12$ ). The two reference solutions are visualized in Fig. 8. We show convergence for both codes as we increase mesh refinement and report the relative  $L^\infty$ -norm of the error compared to the reference solutions on the domain boundary. We also compare the total solve time for both codes on 60-CPU cores. For the same solution accuracy our method is significantly faster than the SPEC code and at least

$N$	$\epsilon_{\text{GMRES}}$	$(N_s + 1) N_{\text{GMRES}}$	$\ e\ _\infty$	$T_{\text{setup}}$	$T_{\text{LB}}$	$T_{\text{quad-eval}}$	$T_{\text{solve}}$
2.0E+3	2.0E-3	78	7.3E-3	0.1	6.8	0.9	7.9
8.1E+3	1.3E-5	104	5.1E-5	1.2	33.7	10.6	45.6
1.8E+4	3.0E-7	119	1.4E-6	5.9	111.8	53.7	171.4
3.2E+4	3.2E-8	129	1.1E-7	13.7	239.7	173.2	426.6
5.1E+4	2.6E-9	139	1.4E-8	26.4	552.6	419.7	998.8

Table 6: Convergence results for our Taylor state solver on a toroidal-shell geometry visualized in Fig. 7 (right). We show convergence in  $\|e\|_\infty$  as we decrease the GMRES tolerance  $\epsilon_{\text{GMRES}}$ , increase the mesh refinement  $N$  and correspondingly increase the quadrature accuracy (using parameters  $M$  and  $q$ ). We also report the number of GMRES iterations  $(N_s + 1) N_{\text{GMRES}}$  and the breakdown of the total solve time  $T_{\text{solve}} \approx T_{\text{setup}} + T_{\text{LB}} + T_{\text{quad-eval}}$  on 60-CPU cores.

an order of magnitude faster for the vacuum field case ( $\lambda = 0$ ). This performance is all the more noteworthy as our solver presently does not take advantage of the 5-fold rotational symmetry about the vertical axis of W7-X, unlike the SPEC code. Note that we have not been able to get results for higher refinement in the SPEC code because the system became ill-conditioned. This is an advantage of our integral formulation, which leads to linear systems which are as well-conditioned as the underlying physical problem.

$\lambda$	BIE method				SPEC code		
	$N$	$\epsilon_{\text{GMRES}}$	$\ e\ _{\infty}$	$T_{\text{solve}}$	$M_{\text{pol}} \times M_{\text{tor}} \times L_{\text{rad}}$	$\ e\ _{\infty}$	$T_{\text{solve}}$
0.0	8.8E+3	3E-02	2.3E-1	0.4	$11 \times 11 \times 5$	3.3E-1	14
	2.5E+4	3E-03	3.1E-2	2.1	$13 \times 13 \times 5$	6.0E-2	38
	3.5E+4	1E-03	6.6E-3	4.3	$15 \times 15 \times 5$	7.9E-3	115
	6.3E+4	3E-04	1.6E-3	11.3	$21 \times 21 \times 5$	1.6E-3	527
	7.9E+4	1E-04	5.9E-4	19.5	-	-	-
	1.9E+5	1E-06	9.4E-6	98.1	-	-	-
	3.5E+5	3E-08	6.7E-7	302.3	-	-	-
	4.7E+5	1E-08	9.0E-8	491.8	-	-	-
	8.2E+5	1E-10	2.0E-9	1651.3	-	-	-
1.0	3.9E+3	1E-01	2.2E-1	1.0	$11 \times 11 \times 5$	3.3E-1	13
	1.6E+4	1E-02	2.6E-2	12.2	$13 \times 13 \times 5$	6.1E-2	38
	2.5E+4	3E-03	7.4E-3	29.8	$15 \times 15 \times 5$	9.1E-3	118
	3.5E+4	1E-03	2.7E-3	61.6	$19 \times 19 \times 5$	3.3E-3	389
	4.8E+4	3E-04	1.2E-3	117.1	$21 \times 21 \times 5$	2.0E-3	541
	7.9E+4	1E-04	2.3E-4	317.9	$23 \times 23 \times 5$	8.5E-4	879
	1.9E+5	1E-06	8.6E-6	1991.0	-	-	-
	2.5E+5	1E-07	9.0E-7	3479.6	-	-	-
	5.2E+5	1E-09	3.0E-8	16763.3	-	-	-
7.7E+5	1E-10	1.7E-9	40646.2	-	-	-	

Table 7: Convergence results for our BIE code and the SPEC code on the W7-X geometry [4, 48]. We show convergence in the relative  $L^{\infty}$ -norm of the error by comparing the solutions with a reference solution. We also report the total solve time  $T_{\text{solve}}$  for both codes on 60-CPU cores. The parameters  $M_{\text{pol}}$ ,  $M_{\text{tor}}$  and  $L_{\text{rad}}$  determine the refinement in the poloidal, toroidal and the radial directions in SPEC. For  $\lambda = 0$ , we use the scheme for vacuum fields described in Section 2.2.4. This has the advantage that it does not require Laplace-Beltrami solves and only requires computing surface convolutions with the Laplace gradient kernel, which is significantly less expensive than computing convolutions with the Helmholtz kernel. We have not been able to obtain results for higher refinement with the SPEC code, because the system became ill-conditioned.

## 5 Summary

In this work, we have developed a solver for computing Taylor relaxed states in toroidal geometries. This extends our previous work in [44] on computing such fields in axisymmetric geometries to non-axisymmetric geometries, and can be applied to the computation of stepped-pressure equilibria in stellarators [34]. The representation of the field using generalized Debye sources [14] remains the same as in the axisymmetric case, but the numerical solver is new. The solver is based on a Fourier pseudo-spectral discretization of the surface.



Figure 8: Reference solutions on the W7X geometry [4, 48] for the convergence results in Table 7. The fields correspond to  $\lambda = 0$  and  $\lambda = 1$  respectively.

We have developed efficient high-order surface quadratures for evaluating layer-potentials based on previous work of [5, 54], but improve on the partition of unity function used to separate the integrals into smooth and singular parts. Our method allows for precomputing the local quadrature resulting in extremely efficient evaluations when used with iterative solvers. We have incorporated other performance optimizations such as shared memory parallelism and vectorization of the kernel functions. We have developed optimized implementations of the Laplace-Beltrami solvers from [35, 43], and have also presented a numerically stable scheme for computing magnetic fluxes for arbitrary values of the Beltrami parameter  $\lambda$  which are critical for our formulation. Finally, we have presented numerical results to show that our method is efficient and high-order accurate.

Since our boundary integral scheme requires only that the boundary of the domain be discretized, and not the entire volume, this significantly reduces the number of unknowns and makes the scheme very efficient. A direct comparison with the existing code SPEC shows that our solver compares favorably, and could be further accelerated, for example, by making use of the usual  $n$ -fold rotational symmetry of stellarator surfaces about the vertical axis as SPEC does (3-fold symmetry for QAS3, 5-fold symmetry for W7-X). We furthermore observe that a boundary integral approach is in fact particularly well-suited for the computation of stepped pressure equilibria because the force balance conditions between adjacent Taylor states need only be evaluated at the ideal MHD interfaces on each iteration, i.e. on the boundaries of the computational domain. Other advantages of our solver include a well-conditioned second-kind integral formulation and no difficulties associated with coordinate singularities (as is common in many volume parameterizations of toroidal domains required in FEM codes). A current limitation of our scheme is that the uniform grid discretization makes it unsuitable for geometries with very sharp features. Such features are frequently required in stellarators to model what are known as *divertors*, used for removing fusion products and impurities in the plasma. Computing Taylor states efficiently in such geometries will require high-order adaptive surface discretizations, alternative singular and near-singular quadratures, more efficient Laplace-Beltrami solvers compatible with such discretizations, and coupling with asymptotically fast solvers, such as fast multipole methods. This is the basis of ongoing research.

## Acknowledgements

The authors would like to thank Stuart Hudson (Princeton Plasma Physics Laboratory) and Joaquim Loizu (Ecole Polytechnique Fédérale de Lausanne) for valuable conversations, for their explanations on how to run the SPEC code, and for sharing their post-processing rou-

tines.

## A Notation

In Table 8, we list some frequently used symbols for easy reference.

Symbol	Description	Symbol	Description
$\Omega$	domain	$\mathcal{F}, \mathcal{F}^{-1}$	periodic Fourier transform and its inverse
$\Gamma$	boundary	$\mathbf{D}_\theta, \mathbf{D}_\varphi$	pseudo-spectral differentiation operators in $\theta$ and $\varphi$ directions
$N_s$	number of surfaces	$g_\lambda(\mathbf{r})$	Helmholtz kernel function
$\theta, \varphi$	toroidal and poloidal angles	$\mathcal{S}_\lambda, \mathcal{D}_\lambda$	Helmholtz single- and double-layer convolution operators
$\mathbf{x}(\theta, \varphi)$	surface position	$M, q$	singular-quadrature parameters
$\mathbf{n}(\theta, \varphi)$	surface normal (outward from $\Omega$ )	$N$	total number of discretization points
$G(\theta, \varphi)$	metric tensor	$N_{LB}$	average number of iterations for each solve of the Laplace Beltrami problem
$\mathbf{B}$	magnetic field	$N_{GMRES}$	average number of iterations for each solve of the boundary integral operator
$\lambda$	Beltrami parameter	$T_{solve}$	total solve time
$S_i, \Phi_i$	domain cross-section and the corresponding flux condition	$T_{setup}$	setup time for singular-quadratures
$N_\theta, N_\varphi$	number of discretization points in toroidal and poloidal directions	$T_{quad-eval}$	evaluation time for the quadratures
$f(\theta, \varphi), \mathbf{f}, \hat{\mathbf{f}}$	function on a surface, its discretization and its Fourier coefficients	$T_{LB}$	Laplace Beltrami solve time

Table 8: Index of frequently used symbols.

## References

- [1] S. Balay, S. Abhyankar, M. F. Adams, J. Brown, P. Brune, K. Buschelman, L. Dalcin, A. Dener, V. Eijkhout, W. D. Gropp, D. Kaushik, M. G. Knepley, D. A. May, L. C. McInnes, R. T. Mills, T. Munson, K. Rupp, P. Sanan, B. F. Smith, S. Zampini, H. Zhang, and H. Zhang. PETSc Web page. <http://www.mcs.anl.gov/petsc>, 2018. URL <http://www.mcs.anl.gov/petsc>.
- [2] S. Balay, S. Abhyankar, M. F. Adams, J. Brown, P. Brune, K. Buschelman, L. Dalcin, A. Dener, V. Eijkhout, W. D. Gropp, D. Kaushik, M. G. Knepley, D. A. May, L. C. McInnes, R. T. Mills, T. Munson, K. Rupp, P. Sanan, B. F. Smith, S. Zampini, H. Zhang, and H. Zhang. PETSc users manual. Technical Report ANL-95/11 - Revision 3.10, Argonne National Laboratory, 2018. URL <http://www.mcs.anl.gov/petsc>.
- [3] F. Bauer, O. Betancourt, and P. Garabedian. *A Computational Method in Plasma Physics*. Springer Berlin Heidelberg, 1978. ISBN 9783642854705. doi: 10.1007/978-3-642-85470-5. URL <http://dx.doi.org/10.1007/978-3-642-85470-5>.
- [4] C. Beidler, G. Grieger, F. Herrnegger, E. Harmeyer, J. Kisslinger, W. Lotz, H. Maassberg, P. Merkel, J. Nührenberg, F. Rau, J. Sapper, F. Sardei, R. Scardovelli, A. Schlüter, and H. Wobig. Physics and Engineering Design for Wendelstein VII-X. *Fusion Technology*,

- 17(1):148–168, 1990. doi: 10.13182/FST90-A29178. URL <https://doi.org/10.13182/FST90-A29178>.
- [5] O. P. Bruno and L. A. Kunyansky. A fast, high-order algorithm for the solution of surface scattering problems: Basic implementation, tests, and applications. *Journal of Computational Physics*, 169(1):80 – 110, May 2001. ISSN 0021-9991. doi: 10.1006/jcph.2001.6714. URL <http://dx.doi.org/10.1006/jcph.2001.6714>.
- [6] O. P. Bruno and L. A. Kunyansky. Surface scattering in three dimensions: an accelerated high-order solver. *Proceedings of the Royal Society A: Mathematical, Physical and Engineering Sciences*, 457(2016):2921 – 2934, Dec 2001. ISSN 1471-2946. doi: 10.1098/rspa.2001.0882. URL <http://dx.doi.org/10.1098/RSPA.2001.0882>.
- [7] O. P. Bruno and P. Laurence. Existence of three-dimensional toroidal MHD equilibria with nonconstant pressure. *Communications on Pure and Applied Mathematics*, 49(7):717 – 764, Jul 1996. ISSN 1097-0312. doi: 10.1002/(sici)1097-0312(199607)49:7<717::aid-cpa3>3.0.co;2-c. URL [http://dx.doi.org/10.1002/\(SICI\)1097-0312\(199607\)49:7<717::AID-CPA3>3.0.CO;2-C](http://dx.doi.org/10.1002/(SICI)1097-0312(199607)49:7<717::AID-CPA3>3.0.CO;2-C).
- [8] A. J. Cerfon and M. O’Neil. Exact axisymmetric Taylor states for shaped plasmas. *Physics of Plasmas*, 21(6):064501, Jun 2014. ISSN 1089-7674. doi: 10.1063/1.4881466. URL <http://dx.doi.org/10.1063/1.4881466>.
- [9] H. Cheng, W. Y. Crutchfield, Z. Gimbutas, L. F. Greengard, J. F. Ethridge, J. n. Huang, V. Rokhlin, N. Yarvin, and J. Zhao. A wideband fast multipole method for the Helmholtz equation in three dimensions. *Journal of Computational Physics*, 216(1):300 – 325, Jul 2006. ISSN 0021-9991. doi: 10.1016/j.jcp.2005.12.001. URL <http://dx.doi.org/10.1016/J.JCP.2005.12.001>.
- [10] W. C. Chew. *Waves and Fields in Inhomogenous Media*. Wiley-IEEE Press, Piscataway, NJ, 1999.
- [11] G. R. Dennis, S. R. Hudson, R. L. Dewar, and M. J. Hole. The infinite interface limit of multiple-region relaxed magnetohydrodynamics. *Physics of Plasmas*, 20(3):032509, Mar 2013. ISSN 1089-7674. doi: 10.1063/1.4795739. URL <http://dx.doi.org/10.1063/1.4795739>.
- [12] M. Drevlak, D. Monticello, and A. Reiman. PIES free boundary stellarator equilibria with improved initial conditions. *Nuclear Fusion*, 45(7):731–740, Jul 2005. ISSN 1741-4326. doi: 10.1088/0029-5515/45/7/022. URL <http://dx.doi.org/10.1088/0029-5515/45/7/022>.
- [13] C. L. Epstein and L. Greengard. Debye Sources and the Numerical Solution of the Time Harmonic Maxwell Equations. *Communications on Pure and Applied Mathematics*, 63(4): 413–463, Apr 2010. doi: 10.1002/cpa.20313. URL <http://dx.doi.org/10.1002/cpa.20313>.
- [14] C. L. Epstein, L. Greengard, and M. O’Neil. Debye Sources and the Numerical Solution of the Time Harmonic Maxwell Equations II. *Communications on Pure and Applied Mathematics*, 66(5):753 – 789, Aug 2012. ISSN 0010-3640. doi: 10.1002/cpa.21420. URL <http://dx.doi.org/10.1002/CPA.21420>.

- [15] C. L. Epstein, L. Greengard, and A. Klöckner. On the convergence of local expansions of layer potentials. *SIAM Journal on Numerical Analysis*, 51(5):2660–2679, Jan 2013. ISSN 1095-7170. doi: 10.1137/120902859. URL <http://dx.doi.org/10.1137/120902859>.
- [16] C. L. Epstein, L. Greengard, and M. O’Neil. Debye Sources, Beltrami Fields, and a Complex Structure on Maxwell Fields. *Commun. Pure Appl. Math.*, 68(12):2237–2280, 2015.
- [17] C. L. Epstein, L. Greengard, and M. O’Neil. A high-order wideband direct solver for electromagnetic scattering from bodies of revolution. 2019. arXiv:1708.00056.
- [18] F. Ethridge and L. Greengard. A New Fast-Multipole Accelerated Poisson Solver in Two Dimensions. *SIAM Journal on Scientific Computing*, 23(3):741 – 760, Jan 2001. ISSN 1095-7197. doi: 10.1137/S1064827500369967. URL <http://dx.doi.org/10.1137/S1064827500369967>.
- [19] M. Frigo and S. Johnson. The design and implementation of FFTW3. *Proceedings of the IEEE*, 93(2):216 – 231, Feb 2005. ISSN 0018-9219. doi: 10.1109/jproc.2004.840301. URL <http://dx.doi.org/10.1109/JPROC.2004.840301>.
- [20] P. R. Garabedian. Three-dimensional codes to design stellarators. *Physics of Plasmas*, 9(1):137–149, 2002. doi: 10.1063/1.1419252. URL <https://doi.org/10.1063/1.1419252>.
- [21] H. Grad. Toroidal containment of a plasma. *Physics of Fluids*, 10(1):137, 1967. ISSN 0031-9171. doi: 10.1063/1.1761965. URL <http://dx.doi.org/10.1063/1.1761965>.
- [22] L. Greengard and V. Rokhlin. A fast algorithm for particle simulations. *Journal of Computational Physics*, 73(2):325 – 348, Dec 1987. ISSN 0021-9991. doi: 10.1016/0021-9991(87)90140-9. URL [http://dx.doi.org/10.1016/0021-9991\(87\)90140-9](http://dx.doi.org/10.1016/0021-9991(87)90140-9).
- [23] K. Harafuji, T. Hayashi, and T. Sato. Computational study of three-dimensional magnetohydrodynamic equilibria in toroidal helical systems. *Journal of Computational Physics*, 81(1):169–192, Mar 1989. ISSN 0021-9991. doi: 10.1016/0021-9991(89)90069-7. URL [http://dx.doi.org/10.1016/0021-9991\(89\)90069-7](http://dx.doi.org/10.1016/0021-9991(89)90069-7).
- [24] T. Hayashi, T. Sato, P. Merkel, J. Nührenberg, and U. Schwenn. Formation and ‘self-healing’ of magnetic islands in finite- $\beta$  helias equilibria. *Physics of Plasmas*, 1(10):3262–3268, Oct 1994. ISSN 1089-7674. doi: 10.1063/1.870478. URL <http://dx.doi.org/10.1063/1.870478>.
- [25] P. Helander. Theory of plasma confinement in non-axisymmetric magnetic fields. *Reports on Progress in Physics*, 77(8):087001, Jul 2014. ISSN 1361-6633. doi: 10.1088/0034-4885/77/8/087001. URL <http://dx.doi.org/10.1088/0034-4885/77/8/087001>.
- [26] S. Hirshman and D. Lee. MOMCON: A spectral code for obtaining three-dimensional magnetohydrodynamic equilibria. *Computer Physics Communications*, 39(2):161–172, Feb 1986. ISSN 0010-4655. doi: 10.1016/0010-4655(86)90127-x. URL [http://dx.doi.org/10.1016/0010-4655\(86\)90127-x](http://dx.doi.org/10.1016/0010-4655(86)90127-x).

- [27] S. Hirshman, W. van RIJ, and P. Merkel. Three-dimensional free boundary calculations using a spectral Green's function method. *Computer Physics Communications*, 43(1):143–155, Dec 1986. ISSN 0010-4655. doi: 10.1016/0010-4655(86)90058-5. URL [http://dx.doi.org/10.1016/0010-4655\(86\)90058-5](http://dx.doi.org/10.1016/0010-4655(86)90058-5).
- [28] S. P. Hirshman and J. C. Whitson. Steepest-descent moment method for three-dimensional magnetohydrodynamic equilibria. *Physics of Fluids*, 26(12):3553, 1983. ISSN 0031-9171. doi: 10.1063/1.864116. URL <http://dx.doi.org/10.1063/1.864116>.
- [29] S. R. Hudson and et. al. Stepped Pressure Equilibrium Code (SPEC). <https://theory.pppl.gov/research/research.php?rid=10#h5>.
- [30] S. R. Hudson and N. Nakajima. Pressure, chaotic magnetic fields, and magnetohydrodynamic equilibria. *Physics of Plasmas*, 17(5):052511, May 2010. ISSN 1089-7674. doi: 10.1063/1.3431090. URL <http://dx.doi.org/10.1063/1.3431090>.
- [31] S. R. Hudson, A. Reiman, D. Strickler, A. Brooks, D. A. Monticello, and S. P. Hirshman. Free-boundary full-pressure island healing in stellarator equilibria: coil-healing. *Plasma Physics and Controlled Fusion*, 44(7):1377–1382, Jun 2002. ISSN 0741-3335. doi: 10.1088/0741-3335/44/7/323. URL <http://dx.doi.org/10.1088/0741-3335/44/7/323>.
- [32] S. R. Hudson, M. J. Hole, and R. L. Dewar. Eigenvalue problems for beltrami fields arising in a three-dimensional toroidal magnetohydrodynamic equilibrium problem. *Physics of Plasmas*, 14(5):052505, May 2007. ISSN 1089-7674. doi: 10.1063/1.2722721. URL <http://dx.doi.org/10.1063/1.2722721>.
- [33] S. R. Hudson, R. L. Dewar, M. J. Hole, and M. McGann. Non-axisymmetric, multi-region relaxed magnetohydrodynamic equilibrium solutions. *Plasma Physics and Controlled Fusion*, 54(1):014005, Dec 2011. ISSN 1361-6587. doi: 10.1088/0741-3335/54/1/014005. URL <http://dx.doi.org/10.1088/0741-3335/54/1/014005>.
- [34] S. R. Hudson, R. L. Dewar, G. Dennis, M. J. Hole, M. McGann, G. von Nessi, and S. Lazerson. Computation of multi-region relaxed magnetohydrodynamic equilibria. *Physics of Plasmas*, 19(11):112502, Nov 2012. ISSN 1089-7674. doi: 10.1063/1.4765691. URL <http://dx.doi.org/10.1063/1.4765691>.
- [35] L.-M. Imbert-Gérard and L. Greengard. Pseudo-Spectral Methods for the Laplace-Beltrami Equation and the Hodge Decomposition on Surfaces of Genus One. *Numerical Methods for Partial Differential Equations*, 33(3):941 – 955, Feb 2017. ISSN 0749-159X. doi: 10.1002/num.22131. URL <http://dx.doi.org/10.1002/NUM.22131>.
- [36] R. Kanno, T. Hayashi, and M. Okamoto. Formation and healing of  $n=1$  magnetic islands in LHD equilibrium. *Nuclear Fusion*, 45(7):588–594, Jun 2005. ISSN 1741-4326. doi: 10.1088/0029-5515/45/7/006. URL <http://dx.doi.org/10.1088/0029-5515/45/7/006>.
- [37] A. Klöckner, A. Barnett, L. Greengard, and M. O 'Neil. Quadrature by expansion: A new method for the evaluation of layer potentials. *Journal of Computational Physics*, 252:332–349, Nov 2013. ISSN 0021-9991. doi: 10.1016/j.jcp.2013.06.027. URL <http://dx.doi.org/10.1016/j.jcp.2013.06.027>.

- [38] J. Loizu, S. R. Hudson, A. Bhattacharjee, S. Lazerson, and P. Helander. Existence of three-dimensional ideal-magnetohydrodynamic equilibria with current sheets. *Physics of Plasmas*, 22(9):090704, Sep 2015. ISSN 1089-7674. doi: 10.1063/1.4931094. URL <http://dx.doi.org/10.1063/1.4931094>.
- [39] J. Loizu, S. R. Hudson, P. Helander, S. A. Lazerson, and A. Bhattacharjee. Pressure-driven amplification and penetration of resonant magnetic perturbations. *Physics of Plasmas*, 23(5):055703, May 2016. ISSN 1089-7674. doi: 10.1063/1.4944818. URL <http://dx.doi.org/10.1063/1.4944818>.
- [40] J. Loizu, S. R. Hudson, and C. Nührenberg. Verification of the SPEC code in stellarator geometries. *Physics of Plasmas*, 23(11):112505, Nov 2016. ISSN 1089-7674. doi: 10.1063/1.4967709. URL <http://dx.doi.org/10.1063/1.4967709>.
- [41] J. Loizu, S. R. Hudson, C. Nührenberg, J. Geiger, and P. Helander. Equilibrium  $\beta$ -limits in classical stellarators. *Journal of Plasma Physics*, 83(06), Nov 2017. ISSN 1469-7807. doi: 10.1017/s0022377817000861. URL <http://dx.doi.org/10.1017/s0022377817000861>.
- [42] D. Malhotra and G. Biros. PVFMM: A Parallel Kernel Independent FMM for Particle and Volume Potentials. *Communications in Computational Physics*, 18(03):808–830, Sep 2015. ISSN 1991-7120. doi: 10.4208/cicp.020215.150515sw. URL <http://dx.doi.org/10.4208/cicp.020215.150515sw>.
- [43] M. O’Neil. Second-kind integral equations for the laplace-beltrami problem on surfaces in three dimensions. *Advances in Computational Mathematics*, Jan 2018. ISSN 1572-9044. doi: 10.1007/s10444-018-9587-7. URL <http://dx.doi.org/10.1007/s10444-018-9587-7>.
- [44] M. O’Neil and A. J. Cerfon. An integral equation-based numerical solver for Taylor states in toroidal geometries. *Journal of Computational Physics*, 359:263 – 282, Apr 2018. ISSN 0021-9991. doi: 10.1016/j.jcp.2018.01.004. URL <http://dx.doi.org/10.1016/J.JCP.2018.01.004>.
- [45] M. Rachh, A. Klöckner, and M. O’Neil. Fast algorithms for quadrature by expansion i: Globally valid expansions. *Journal of Computational Physics*, 345:706–731, Sep 2017. ISSN 0021-9991. doi: 10.1016/j.jcp.2017.04.062. URL <http://dx.doi.org/10.1016/j.jcp.2017.04.062>.
- [46] A. Reiman and H. Greenside. Numerical solution of three-dimensional magnetic differential equations. *Journal of Computational Physics*, 75(2):423–443, Apr 1988. ISSN 0021-9991. doi: 10.1016/0021-9991(88)90121-0. URL [http://dx.doi.org/10.1016/0021-9991\(88\)90121-0](http://dx.doi.org/10.1016/0021-9991(88)90121-0).
- [47] A. Reiman, N. Ferraro, A. Turnbull, J. Park, A. Cerfon, T. Evans, M. Lanctot, E. Lazarus, Y. Liu, G. McFadden, D. Monticello, and Y. Suzuki. Tokamak plasma high field side response to an  $n=3$  magnetic perturbation: a comparison of 3D equilibrium solutions from seven different codes. *Nuclear Fusion*, 55(6):063026, May 2015. ISSN 1741-4326. doi: 10.1088/0029-5515/55/6/063026. URL <http://dx.doi.org/10.1088/0029-5515/55/6/063026>.

- [48] T. Sunn Pedersen, A. Dinklage, Y. Turkin, R. Wolf, S. Bozhnikov, J. Geiger, G. Fuchert, H.-S. Bosch, K. Rahbarnia, H. Thomsen, U. Neuner, T. Klinger, A. Langenberg, H. Trimiño Mora, P. Kornejew, J. Knauer, M. Hirsch, and N. Pablant. Key results from the first plasma operation phase and outlook for future performance in Wendelstein 7-X. *Physics of Plasmas*, 24(5):055503, 2017. doi: 10.1063/1.4983629. URL <https://doi.org/10.1063/1.4983629>.
- [49] Y. Suzuki, N. Nakajima, K. Watanabe, Y. Nakamura, and T. Hayashi. Development and application of HINT2 to helical system plasmas. *Nuclear Fusion*, 46(11):L19–L24, Sep 2006. ISSN 1741-4326. doi: 10.1088/0029-5515/46/11/101. URL <http://dx.doi.org/10.1088/0029-5515/46/11/101>.
- [50] P. Swarztrauber. FFTPACK, a package of FORTRAN subprograms for the fast fourier transform of periodic and other symmetric sequences. *Siehe: <http://netlib.org/fftpack>*, 1985.
- [51] J. B. Taylor. Relaxation of toroidal plasma and generation of reverse magnetic fields. *Physical Review Letters*, 33(19):1139–1141, Nov 1974. ISSN 0031-9007. doi: 10.1103/physrevlett.33.1139. URL <http://dx.doi.org/10.1103/PhysRevLett.33.1139>.
- [52] M. Taylor. A high performance spectral code for nonlinear MHD stability. *Journal of Computational Physics*, 110(2):407–418, Feb 1994. ISSN 0021-9991. doi: 10.1006/jcph.1994.1035. URL <http://dx.doi.org/10.1006/jcph.1994.1035>.
- [53] L. Ying, G. Biros, and D. Zorin. A kernel-independent adaptive fast multipole algorithm in two and three dimensions. *Journal of Computational Physics*, 196(2):591 – 626, May 2004. ISSN 0021-9991. doi: 10.1016/j.jcp.2003.11.021. URL <http://dx.doi.org/10.1016/j.jcp.2003.11.021>.
- [54] L. Ying, G. Biros, and D. Zorin. A high-order 3D boundary integral equation solver for elliptic PDEs in smooth domains. *Journal of Computational Physics*, 219(1):247 – 275, Nov 2006. ISSN 0021-9991. doi: 10.1016/j.jcp.2006.03.021. URL <http://dx.doi.org/10.1016/j.jcp.2006.03.021>.